

# Spectroscopic Definition of the $\text{Cu}_2^{\circ}$ Intermediate in Turnover of Nitrous Oxide Reductase and Molecular Insight into the Catalytic Mechanism

Esther M. Johnston,<sup>#,†</sup> Cíntia Carreira,<sup>%</sup> Simone Dell'Acqua,<sup>%,‡</sup> Somdatta Ghosh Dey,<sup>#, &</sup> Sofia R. Pauleta,<sup>%,</sup> Isabel Moura,<sup>%,</sup> and Edward I. Solomon<sup>#, \*</sup>

<sup>#</sup>Department of Chemistry, Stanford University, Stanford, CA. <sup>%</sup>UCIBIO, REQUIMTE, Departamento de Química, Faculdade de Ciências e Tecnologia, Universidade Nova de Lisboa, Campus da Caparica, 2829-516 Caparica, Portugal.

**Keywords:** Nitrous oxide reductase; active form; catalytic cycle;  $\text{Cu}_2$  center; Copper enzyme; Intermediate species

**ABSTRACT:** An intermediate 1-hole (i.e.  $3\text{Cu}^{\text{I}}\text{Cu}^{\text{II}}$ ) form of the tetranuclear copper monosulfide ( $\text{Cu}_4\text{S}$ ) active site of nitrous oxide reductase ( $\text{N}_2\text{OR}$ ), which differs from the resting 1-hole  $\text{Cu}_2^*$  state, has been observed in single turnover of fully reduced  $\text{N}_2\text{OR}$  with  $\text{N}_2\text{O}$ . In this study, we show that this  $\text{Cu}_2^{\circ}$  intermediate can be reduced via electron transfer from  $\text{Cu}_A$  using a physiologically relevant reductant, sodium ascorbate, and a lower limit on the rate of this intramolecular electron transfer (IET) that is  $>10^4$  faster than the unobserved IET for resting  $\text{Cu}_2^*$  is obtained. A combination of spectroscopic methods and density functional theory (DFT) calculations are used to determine the geometric and electronic structure of  $\text{Cu}_2^{\circ}$ . Electron paramagnetic resonance (EPR), absorption, and magnetic circular dichroism (MCD) spectroscopies show that there is a redistribution of spin density in the  $\text{Cu}_4\text{S}$  cluster from localized  $\sim 5:2$  over  $\text{Cu}_I$  and  $\text{Cu}_{IV}$  in resting 1-hole  $\text{Cu}_2^*$  to delocalized 1:1 over  $\text{Cu}_I$  and  $\text{Cu}_{IV}$  in the  $\text{Cu}_2^{\circ}$  intermediate. Two Cu-S vibrations are observed in the resonance Raman spectrum at 425 and 413  $\text{cm}^{-1}$ , higher energy than in  $\text{Cu}_2^*$ . The latter shows an  $\text{O}^{18}$  solvent isotope shift, indicating that  $\text{Cu}_2^{\circ}$  has an exchangeable hydroxide ligand. DFT calculations are used to correlate these spectral features to a model for the  $\text{Cu}_2^{\circ}$  intermediate having a terminal hydroxide ligand coordinated to  $\text{Cu}_{IV}$ , stabilized by a hydrogen bond to a nearby lysine residue. Marcus theory is used to determine that the catalytically competent reduction of  $\text{Cu}_2^{\circ}$  in turnover is due to its being a higher energy metastable state relative to resting  $\text{Cu}_2^*$ . Terminal hydroxide coordination to  $\text{Cu}_{IV}$  in the  $\text{Cu}_2^{\circ}$  intermediate yields insight into the nature of  $\text{N}_2\text{O}$  binding and reduction, specifying a molecular mechanism in which  $\text{N}_2\text{O}$  coordinates in a  $\mu\text{-}1,3$  fashion to the fully reduced state, with hydrogen bonding from Lys397, and two electrons are transferred from the fully reduced  $\text{Cu}_4\text{S}$  cluster to  $\text{N}_2\text{O}$  via a single Cu atom from the  $\mu_4\text{S}^{2-}$  bridged tetranuclear copper cluster to accomplish N-O bond cleavage.

## 1. Introduction.

The mitigation of man-made pollution of the global atmosphere is one of the most important scientific challenges of the 21<sup>st</sup> century. Nitrous oxide ( $\text{N}_2\text{O}$ ) emissions from anthropogenic sources are important contributors to global warming, as  $\text{N}_2\text{O}$  has 300 times the global warming potential of  $\text{CO}_2$ ,<sup>1</sup> and also contributes to the depletion of the ozone layer.<sup>2</sup> Two-thirds of anthropogenic  $\text{N}_2\text{O}$  emissions arise from agricultural soils,<sup>3,4</sup> where  $\text{N}_2\text{O}$  is formed as part of the bacterial denitrification pathway, in which soil and marine bacteria use oxidized nitrogen compounds as terminal electron acceptors for anaerobic respiration.<sup>5</sup> Many bacterial denitrifiers contain the enzyme nitrous oxide reductase ( $\text{N}_2\text{OR}$ ), which catalyzes the two electron and two proton reduction of  $\text{N}_2\text{O}$  to  $\text{N}_2$  and  $\text{H}_2\text{O}$ , as the terminal step of denitrification, thus preventing the environmental release of  $\text{N}_2\text{O}$ .<sup>6,7</sup> This reaction is exergonic by 81 kcal/mol but kinetically hindered by a high barrier for N-O bond cleavage (+59 kcal/mol in the gas phase), thus requiring enzymatic catalysis.<sup>8</sup> Understanding the molecular mechanism by which  $\text{N}_2\text{OR}$  catalyzes this reaction *in vivo* could contribute to efforts to mitigate the environmental release of  $\text{N}_2\text{O}$ .<sup>3</sup>

$\text{N}_2\text{OR}$  is a homodimeric metalloenzyme that contains two copper sites: a binuclear copper site known as  $\text{Cu}_A$ , which receives an electron from cytochrome *c* or cupredoxin and transfers it to a unique tetranuclear copper monosulfide ( $\text{Cu}_4\text{S}$ ) active site, where  $\text{N}_2\text{O}$  binds and is reduced (Figure 1).<sup>9-13</sup> The two copper sites are separated by a distance of 10 Å across the dimer interface and a solvent-filled cavity lies between them.  $\text{Cu}_A$  is ligated equatorially by two bridging Cys and two His residues and is structurally and electronically similar to an equivalent electron transfer site in the enzyme cytochrome *c* oxidase.<sup>14,15</sup> The  $\text{Cu}_4\text{S}$  active site is ligated by 7 His residues and contains three copper atoms (designated  $\text{Cu}_I$ ,  $\text{Cu}_{II}$ , and  $\text{Cu}_{IV}$ ) that share a plane with the  $\mu_4\text{S}^{2-}$  sulfide ligand and with a solvent-derived ligand that bridges the  $\text{Cu}_I$ - $\text{Cu}_{IV}$  edge, while the fourth copper ( $\text{Cu}_{III}$ ) bound to the  $\mu_4\text{S}^{2-}$  is oriented out of this plane. The resting state of the  $\text{Cu}_4\text{S}$  cluster, known as  $\text{Cu}_2^*$ , has been extensively characterized by spectroscopic methods and has a mixed valent  $3\text{Cu}^{\text{I}}\text{Cu}^{\text{II}}$  (1-hole) electronic structure, where the hole is delocalized in a  $\sim 5:2$  ratio over two coppers in the cluster,  $\text{Cu}_I$  and  $\text{Cu}_{IV}$ , respectively.<sup>16-19</sup> Studies of the pH dependence of the resting 1-hole  $\text{Cu}_2^*$  state show that in this state the solvent-

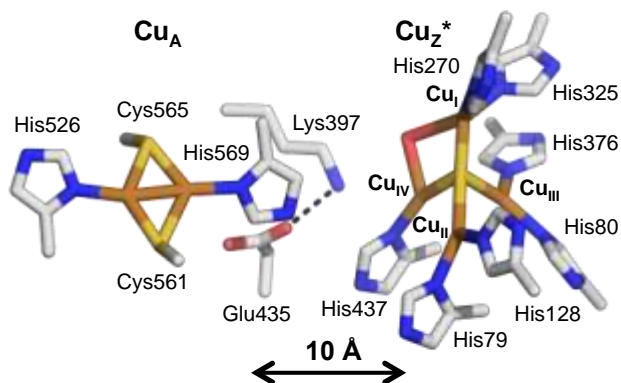


Figure 1: A) X-ray crystallographic structure of the copper sites of nitrous oxide reductase from *Paracoccus denitrificans* (1FWX, resolution 1.7 Å),<sup>22</sup> identifying important ligating and second sphere residues.

exchangeable  $\text{Cu}_I$ - $\text{Cu}_{IV}$  edge ligand is a hydroxide, which changes position depending on the protonation state of the second sphere residue Lys397 (Figure 1).<sup>20</sup> An alternative two sulfur ( $\text{Cu}_4\text{S}_2$ ) form of the  $\text{N}_2\text{OR}$  active site has been observed when  $\text{N}_2\text{OR}$ s from *Pseudomonas stutzeri* and *Marinobacter hydrocarbonoclasticus* ( $Mh\text{N}_2\text{OR}$ , used in this study) are isolated under low dioxygen conditions.<sup>21,22</sup> However, single turnover studies have shown that none of the accessible redox states of the  $\text{Cu}_4\text{S}_2$  cluster react rapidly with  $\text{N}_2\text{O}$ ,<sup>23</sup> while the fully reduced ( $4\text{Cu}^I$ ) state of the  $\text{Cu}_4\text{S}$  cluster does react with  $\text{N}_2\text{O}$  at a sufficiently rapid rate to be catalytically relevant.<sup>24</sup> The  $4\text{Cu}^I$  state of the  $\text{Cu}_4\text{S}$  cluster is also responsible for turnover in the standard steady-state assay for  $\text{N}_2\text{OR}$  activity, which uses the electron donor methyl viologen.<sup>23,25</sup>

Despite the evidence that the  $4\text{Cu}^I$  state of the  $\text{Cu}_4\text{S}$  cluster is the only form of the  $\text{N}_2\text{OR}$  active site that can reduce  $\text{N}_2\text{O}$  at a rate that is catalytically competent for turnover,<sup>23</sup> important questions remain. Specifically, the putative reactive  $4\text{Cu}^I$  state can only be accessed *in vitro* from the resting 1-hole  $\text{Cu}_Z^*$  state via a slow reductive activation using dithionite-reduced viologen reductants (methyl or benzyl viologen), and not with physiologically relevant reductants, such as cytochrome  $c_{552}$ , the physiological electron donor of  $Mh\text{N}_2\text{OR}$ , or sodium ascorbate.<sup>25,26</sup> This calls into question whether the reactive  $4\text{Cu}^I$  state of the  $\text{Cu}_4\text{S}$  cluster can be accessed *in vivo*; indeed, the reduction of resting 1-hole  $\text{Cu}_Z^*$  to the  $4\text{Cu}^I$  state is too slow to be part of the catalytic cycle. However, an alternative oxidized state of the  $\text{Cu}_4\text{S}$  cluster, known as  $\text{Cu}_Z^0$ , has been observed as a transient intermediate in the single turnover reaction of fully reduced  $\text{N}_2\text{OR}$  with  $\text{N}_2\text{O}$ .<sup>27</sup> In contrast to resting 1-hole  $\text{Cu}_Z^*$ ,  $\text{Cu}_Z^0$  is reduced rapidly in steady-state experiments with methyl viologen. The  $\text{Cu}_Z^0$  intermediate shows an  $S=1/2$  EPR signal, indicating that it is a 1-hole state of the  $\text{Cu}_4\text{S}$  cluster, and an absorption maximum at 680 nm, red-shifted from the absorption maximum of resting 1-hole  $\text{Cu}_Z^*$ , which is at 640 nm.<sup>27</sup> Characterization of the  $\text{Cu}_Z^0$  intermediate to determine its geometric and electronic structure and reactivity with physiologically relevant reductants is essential to elucidate how it differs from the resting 1-hole form of  $\text{Cu}_Z^*$  and understand its role in the mechanism of  $\text{N}_2\text{O}$  reduction.

In this study, EPR, absorption, MCD, and resonance Raman spectroscopies are performed on freeze-trapped samples of the  $\text{Cu}_Z^0$  intermediate to characterize its electronic structure. We then use DFT calculations to develop a structural model for this intermediate that is consistent with this electronic structure and with the differences in spectral features of  $\text{Cu}_Z^0$  relative to resting 1-hole  $\text{Cu}_Z^*$ . We further determine that the  $\text{Cu}_Z^0$  intermediate can be rapidly reduced to the reactive  $4\text{Cu}^I$  state via electron transfer from  $\text{Cu}_A$  using a physiologically relevant reductant, sodium ascorbate, and use our computational model to elucidate the structural and energetic basis for the rapid reduction of  $\text{Cu}_Z^0$  but not of the resting 1-hole  $\text{Cu}_Z^*$  by  $\text{Cu}_A$  in turnover. This establishes that the  $\text{Cu}_Z^0$  intermediate is the relevant 1-hole oxidized form of the  $\text{Cu}_4\text{S}$  cluster in the turnover and reduction of  $\text{N}_2\text{O}$ , bypassing the inactive resting 1-hole  $\text{Cu}_Z^*$  state. We further extend the structural insight gained from the  $\text{Cu}_Z^0$  intermediate to examine the nature of  $\text{N}_2\text{O}$  binding and reduction in the catalytic mechanism of  $\text{N}_2\text{OR}$ .

## 2. Methodology.

**2.1 Materials:** All reagents were of the highest grade commercially available and used without further purification. Buffers and reductants were purchased from Sigma-Aldrich. 10%  $\text{N}_2\text{O}$  in argon was obtained from Praxair.  $\text{D}_2\text{O}$  (99.9% D), deuterated glycerol (98% D), and  $\text{H}_2\text{O}^{18}$  (97%  $\text{O}^{18}$ ) were purchased from Cambridge Isotopes.

**2.2 Isolation of nitrous oxide reductase:** Nitrous oxide reductase was purified from *Marinobacter hydrocarbonoclasticus* 617 (previously named *Pseudomonas nautica*) according to previously published procedures.<sup>22</sup> The cells were grown anaerobically in the presence of nitrate, and  $Mh\text{N}_2\text{OR}$  was purified under aerobic conditions without added reductant, using a three step column procedure that has been shown to result in  $Mh\text{N}_2\text{OR}$  that contains dominantly the monosulfide  $\text{Cu}_4\text{S}$ , resting 1-hole  $\text{Cu}_Z^*$ , cluster, with the presence of a minimal amount of the disulfide  $\text{Cu}_4\text{S}_2$  form.<sup>22,23</sup> The amount of the  $\text{Cu}_4\text{S}$  cluster present in the purified  $Mh\text{N}_2\text{OR}$  used for this study was determined by EPR spin quantitation before and after methyl viologen reduction (which results in reduction of all copper sites except the 1-hole state of the  $\text{Cu}_4\text{S}_2$  cluster).  $90\pm 10\%$  or  $80\pm 10\%$  of the total tetranuclear cluster concentration was determined to be the  $\text{Cu}_4\text{S}$  form and  $10\pm 10\%$  or  $20\pm 10\%$  was determined to be the  $\text{Cu}_4\text{S}_2$  form of the cluster. The purified enzyme was stored in 100 mM Tris-HCl at a pH 7.6 in liquid nitrogen until further use. The two enzyme preparations used in this study have specific activities of  $180 \pm 17$  and  $190 \pm 20 \mu\text{mol N}_2\text{O min}^{-1} \text{mg}^{-1}$  for the 80% and 90%  $\text{Cu}_4\text{S}$   $Mh\text{N}_2\text{OR}$ , respectively, at pH 7.6.

**2.3 Spectroscopic sample preparation and instrumentation:** Fully reduced  $\text{Cu}_4\text{S}$ -containing  $Mh\text{N}_2\text{OR}$  samples were prepared in a glove box under  $\text{N}_2$  atmosphere.  $Mh\text{N}_2\text{OR}$  in 100 mM pH 7.6 phosphate buffer was reduced by incubation with a 100-fold excess of sodium dithionite-reduced methyl viologen. After 1-2 hours of reduction, the excess reductant was removed by PD-10 Sephadex G-25 desalting column and the protein-containing fractions were concentrated by centrifugation. Fully reduced samples were transferred out of the glove box in tightly capped absorption cuvettes, conical

vials, or EPR tubes and immediately used for spectroscopic sample preparation.

The reaction of fully reduced *MhN<sub>2</sub>OR* with N<sub>2</sub>O was initiated by adding a stoichiometric amount of N<sub>2</sub>O from a solution of 2.5 mM N<sub>2</sub>O in 100 mM pH 7.6 phosphate buffer, obtained by saturation of the buffer with 10% N<sub>2</sub>O in argon at room temperature. 10-15  $\mu$ L of the 2.5 mM N<sub>2</sub>O solution were typically added to ~250  $\mu$ L of fully reduced *MhN<sub>2</sub>OR* for 0.10-0.30 mM concentrations of Cu<sub>2</sub><sup>o</sup>. Complete mixing was obtained by vigorously shaking or vortexing the reaction mixture for 15-30 seconds. Absorption spectra of Cu<sub>2</sub><sup>o</sup> were obtained by performing the N<sub>2</sub>O reaction in a quartz cuvette at room temperature. The reaction progress was monitored with an Agilent 8453 UV-vis spectrophotometer with deuterium and tungsten sources. The first absorption spectrum of Cu<sub>2</sub><sup>o</sup> was obtained at 30 seconds after the initial addition of N<sub>2</sub>O.

Samples for electron paramagnetic resonance (EPR) and resonance Raman spectroscopy of Cu<sub>2</sub><sup>o</sup> were prepared by carrying out the N<sub>2</sub>O reaction with 0.1-0.5 mM fully reduced N<sub>2</sub>OR in a quartz EPR tube, which was vortexed for 15-30 seconds and immediately frozen in an acetone/dry ice bath. After freezing, samples were transferred to liquid nitrogen for storage and data collection. X band EPR spectra were collected using a Bruker EMX spectrometer with an ER 041 XG microwave bridge and an ER4102ST sample cavity. X-band samples were run at 77 K using a liquid nitrogen finger dewar. EPR spectra were baseline corrected using the WinEPR program (Bruker) and simulated using the XSophe program (Bruker). Resonance Raman spectra were collected using a series of lines from a Kr<sup>+</sup> ion laser (Coherent 190CK), a Ti-sapphire laser (M-squared Solstice, pumped by a 12 W Lighthouse Photonics Sprout diode pumped solid state laser), and a Dye laser (Rhodamine 6G, Coherent 699) with incident power of 20-30 mW arranged in a 130° backscattering configuration. The scattered light was dispersed through a triple monochromator (Spex 1877 CP, with 1200, 1800, and 2400 grooves mm<sup>-1</sup> gratings) and detected with a back-illuminated CCD camera (Andor iDus model). Samples prepared in EPR tubes were immersed in a liquid nitrogen finger dewar at 77 K for resonance Raman experiments. The intensity of the ice peak at ~229 cm<sup>-1</sup> was used to normalize the intensities of vibrations to obtain resonance Raman excitation profiles. The spectrum of carbon black in an identical quartz EPR tube was subtracted to remove the spectral contribution from quartz scattering.

Samples for magnetic circular dichroism (MCD) spectroscopy were prepared by premixing 0.1-0.3 mM fully reduced *MhN<sub>2</sub>OR* with 50% deuterated glycerol and preparing a 2.5 mM N<sub>2</sub>O solution in 1:1 deuterated glycerol to 100 mM phosphate buffer at pD 7.6. Upon addition of a stoichiometric amount of the N<sub>2</sub>O solution to fully reduced *MhN<sub>2</sub>OR* in 50% glycerol, the reaction was mixed with a syringe for ~30 s, then transferred to an MCD cell and frozen in an acetone/dry ice bath at -80°C. Parallel MCD samples of fully reduced *MhN<sub>2</sub>OR* were prepared by adding glycerol-buffer solutions that did not contain N<sub>2</sub>O. These were used to determine the spectral contribution of the residual unreduced 1-hole Cu<sub>4</sub>S<sub>2</sub> cluster. MCD spectra were collected on CD spectropolarimeters (Jasco J810 with an S20 PMT detector for the

300-900 nm region and a Jasco J730 with an InSb detector for the 600-2000 nm region) with sample compartments modified to insert a magnetocryostat (Oxford Instruments SM4-7T).

**2.4 Reactivity and steady-state kinetics:** Fully reduced N<sub>2</sub>OR was prepared by incubation with 100 equivalents of reduced methyl viologen in 100 mM Tris-HCl pH 7.6 for 3 hours. Reductants were removed in a NAP-5 column equilibrated with 100 mM pH 7.6 phosphate buffer and the protein concentration was determined by the Pierce Method. To study the reduction of Cu<sub>2</sub><sup>o</sup> by sodium ascorbate, typically 20  $\mu$ M fully reduced N<sub>2</sub>OR was reacted with 36  $\mu$ M N<sub>2</sub>O to form Cu<sub>2</sub><sup>o</sup> in a stirred absorption cell. After 37 seconds of reaction with N<sub>2</sub>O, a solution containing sodium ascorbate was added (final concentration of 7.29 mM, 366-fold molar excess) to the cuvette under agitation. The reduction was followed by absorption spectroscopy, using a TIDAS diode-array spectrophotometer and spectra were collected for at least 1 hour inside a Braun anaerobic box. A parallel experiment using sodium ascorbate to reduce *MhN<sub>2</sub>OR* containing resting 1-hole Cu<sub>2</sub><sup>\*</sup> and oxidized Cu<sub>A</sub> was performed as above with 16.5  $\mu$ M N<sub>2</sub>OR and 7.5 mM sodium ascorbate. An additional experiment was performed in which fully reduced N<sub>2</sub>OR was added to a stirred cell containing sodium ascorbate and N<sub>2</sub>O (final concentrations: 20  $\mu$ M N<sub>2</sub>OR, 10 mM ascorbate, and 0.2 mM N<sub>2</sub>O). Control experiments to monitor changes in fully reduced N<sub>2</sub>OR in the absence and presence of sodium ascorbate were also performed (no absorbance changes was observed over time, data not shown). All these experiments were performed with a sample of *MhN<sub>2</sub>OR* containing 80% of the Cu<sub>4</sub>S and 20% of the Cu<sub>4</sub>S<sub>2</sub> cluster.

The dependence of the steady-state activity of *MhN<sub>2</sub>OR* on pH, pD, and temperature was determined. Steady-state activity measurements were performed by monitoring the oxidation of reduced methyl viologen, following published procedures.<sup>9</sup> *MhN<sub>2</sub>OR* was activated at the optimum pH for reduction by incubating with 500-fold excess of dithionite reduced methyl viologen in the glove box at room temperature for at least an hour in 100 mM pH 7.3 phosphate buffer. An aliquot of this solution was then added to an anaerobic solution of excess methyl viologen and dithionite (in a cuvette under agitation) at the appropriate pH, pD, or temperature. N<sub>2</sub>O saturated water was immediately added to initiate the steady-state turnover reaction. There is a 10% error in activity measurements obtained by this method. Typically 3 replicates were performed at each pH and pD, while six replicates were performed at each temperature. pH and pD activity values reported are the average of multiple replicates with the appropriate propagation of errors. The log of the initial rate of oxidation of reduced methyl viologen (k or k/T) was plotted relative to 1/T to obtain thermodynamic parameters for the rate determining step of steady-state turnover in *MhN<sub>2</sub>OR*.

**2.5 Computational Methods:** A computational model of the Cu<sub>4</sub>S active site was built from the atomic coordinates of the crystal structure of *PdN<sub>2</sub>OR* (PDB ID 1FWX, residue numbers from *MhN<sub>2</sub>OR*), as it is the highest resolution structure available of N<sub>2</sub>OR (resolution 1.6 Å). The model included the active site core (Cu<sub>4</sub>S), the edge hydroxide, 7 ligating histidines,

and the second sphere residues Lys397 and Glu435 (Figure 1). All protein residues were included up to the  $\alpha$  carbons, which were constrained at their crystallographic positions. The distal nitrogen of each His ligand, which is typically involved in a hydrogen bond to a second sphere residue or the protein backbone, was also fixed in place. Additionally, the distant oxygen of Glu435 was constrained in its crystallographic position. (In optimizations including an unconstrained Glu435, this residue moves significantly from its crystallographic position to form a hydrogen bond to His437, a  $\text{Cu}_{\text{IV}}$  ligand.) Calculations were performed using Gaussian 09 (version d01).<sup>28</sup> Molecular structures and frequencies were visualized using Avogadro, an open source molecular builder and visualization tool (Version 1.1.1).<sup>29</sup> LUMO version 1.0.<sup>30</sup> and VMD 1.9.1<sup>31</sup> were used to visualize molecular orbitals and QMForge was used to obtain Mulliken spin populations of different orbitals.<sup>32</sup> Geometry optimizations were performed using B3LYP and BP86 with 10% Hartree-Fock exchange, the TZVP basis set on all core atoms ( $\text{Cu}_4\text{S}$ ), the ligating His nitrogens, the edge ligand and atoms involved in the Lys397-Glu435 hydrogen bonding network ( $\text{NH}_3^+$  or  $\text{NH}_2$  of Lys397 and  $\text{CO}_2$  of Glu435), and the SV basis set on all remaining atoms. Optimizations were performed in a PCM of 10 to ensure that the proton involved in the Lys397-Glu435 hydrogen bond remains on Lys397 (PCM values less than 8 yield a neutral Lys397 Glu435-H as the lowest energy structure). Optimized structures were then used for frequency calculations. In the analysis of vibrational frequencies of the  $\text{Cu}_I\text{-OH}_2\text{-Cu}_{\text{IV}}$  and  $\text{Cu}_{\text{IV}}\text{-OH}$  models of  $\text{Cu}_2^\circ$ , significant mixing was observed between high energy Cu-S stretching modes and His methylene bending modes. To remove this computational artifact, the  $\alpha$  carbons of His residues involved in this mixed were increased in mass until pure Cu-S vibrations were obtained.<sup>33</sup>

The decay process of the  $\text{Cu}_{\text{IV}}\text{-OH}$  model of  $\text{Cu}_2^\circ$  to resting 1-hole  $\text{Cu}_2^*$ , with an OH bridged edge, was calculated by performing a 1D potential energy scan with a constrained  $\text{Cu}_I\text{-OH}$  and  $\text{Cu}_I\text{-Cu}_{\text{IV}}$  distance of 3.6 Å (to reflect the larger  $\text{Cu}_I\text{-Cu}_{\text{IV}}$  distance observed crystallographically for resting  $\text{Cu}_2^*$ ) and a transition state was obtained for this process. The process is close to barrier-less when the  $\text{Cu}_I\text{-Cu}_{\text{IV}}$  distance is not constrained.

To obtain a starting structure for the N-O bond cleavage coordinate,  $\text{N}_2\text{O}$  was positioned near an optimized fully reduced model of the cluster.<sup>8,34</sup> Initial geometries investigated included  $\mu\text{-}1,3$  coordination of  $\text{N}_2\text{O}$  (with the O on both  $\text{Cu}_I$  and  $\text{Cu}_{\text{IV}}$ ),  $\mu\text{-}1,1\text{-O}$  coordination, and terminal coordination of a linear  $\text{N}_2\text{O}$  molecule to  $\text{Cu}_I$  or  $\text{Cu}_{\text{IV}}$  through either the N or O. Stationary points were only found for end-on N coordination to  $\text{Cu}_I$  and for  $\mu\text{-}1,3$  bent coordination with the O coordinated to  $\text{Cu}_{\text{IV}}$  (using BP86 with 10% Hartree-Fock; B3LYP has no stationary point for this structure). In the N-O bond elongation coordinate for the terminal  $\text{Cu}_I\text{-N}_2\text{O}$  structure, the  $\text{N}_2\text{O}$  molecule undergoes an early rearrangement with no barrier to form a  $\mu\text{-}1,3$  coordinated bent  $\text{N}_2\text{O}$  that proceeds in N-O bond cleavage as found for the  $\mu\text{-}1,3$  structure obtained with BP86 and 10% Hartree-Fock. The  $\mu\text{-}1,3$  bound  $\text{N}_2\text{O}$  structure obtained with BP86 and 10% Hartree-Fock exchange was used as the starting point for a 1D potential en-

ergy scan of N-O bond elongation, leading to a transition state for this process. The  $\mu\text{-}1,3$   $\text{N}_2\text{O}$  structure was also used to generate 2D and 3D potential energy surfaces for N-O bond cleavage, proton transfer from Lys397 to O, and  $\text{Cu}_I\text{-N}$  bond cleavage.

### 3. Results and Analysis.

**3.1 Spectroscopy of  $\text{Cu}_2^\circ$ :** The reaction of fully reduced  $Mh\text{N}_2\text{OR}$  with stoichiometric  $\text{N}_2\text{O}$  (in the absence of additional reductant) results in the rapid formation of the intermediate  $\text{Cu}_2^\circ$ , concomitant with oxidation of  $\text{Cu}_A$ .<sup>27</sup> The kinetics of formation ( $k_f = 200 \text{ s}^{-1}$ )<sup>23</sup> and decay ( $k_{\text{decay}} = 0.005 \text{ s}^{-1}$ )<sup>27</sup>, previously reported for the  $\text{Cu}_2^\circ$  intermediate, indicate that samples trapped in less than two minutes will contain mainly  $\text{Cu}_2^\circ$  (Figure S1). Accounting for all the species in the reaction mixture, spectra of samples trapped in 50-60 s (Figure S2, black) contain contributions from three species: the  $\text{Cu}_2^\circ$  intermediate (68%), oxidized  $\text{Cu}_A$  (68%), and residual 1-hole  $\text{Cu}_4\text{S}_2$   $\text{Cu}_Z$  (~10% present for the  $\text{N}_2\text{OR}$  preparation used here). The spectral features of  $\text{Cu}_2^\circ$  were cleanly distinguished from the mixtures by removing the spectral contributions of 1-hole  $\text{Cu}_Z$  and oxidized  $\text{Cu}_A$ . The spectral contribution of residual 1-hole  $\text{Cu}_4\text{S}_2$   $\text{Cu}_Z$  was determined from samples of the methyl viologen reduced protein (shown in Ref. <sup>23</sup> to reduce all copper sites except the 1-hole  $\text{Cu}_4\text{S}_2$   $\text{Cu}_Z$  cluster) that were prepared in parallel with the intermediate samples (Figure S2, blue). The spectral contribution of oxidized  $\text{Cu}_A$  was determined by subtracting the spectrum of oxidized resting  $Mh\text{N}_2\text{OR}$  from that of ascorbate-reduced  $Mh\text{N}_2\text{OR}$  (which from Ref. <sup>23</sup> reduces only  $\text{Cu}_A$ ) and scaling the resulting  $\text{Cu}_A$  spectrum to the appropriate concentration (Figure S2, red). For the EPR and MCD spectra, fit versions of the  $\text{Cu}_A$  spectra were used for these subtractions.

**3.1.1 EPR:** The X band EPR spectrum of  $\text{Cu}_2^\circ$  obtained using this approach is axial with  $g_{\parallel} > g_{\perp} > 2.0023$ , indicating a  $d_{x^2-y^2}$  ground state. Six hyperfine features can be discerned, showing that the unpaired spin is delocalized over more than one Cu (Figure 2, black, with simulation shown in red).

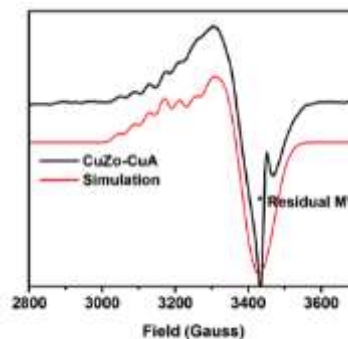


Figure 2: EPR spectrum of  $\text{Cu}_2^\circ$  at 77 K (black) after subtraction of 1-hole  $\text{Cu}_Z$  and an equal spin integration of oxidized  $\text{Cu}_A$ , with fit (red). MV, reduced methyl viologen.

The EPR spectrum of  $\text{Cu}_2^\circ$  was fit with similar  $g$  values to those previously obtained for resting 1-hole  $\text{Cu}_2^*$  (Table 1), consistent with the results obtained by Dell'Acqua et. al.<sup>27</sup> However, we are additionally able to resolve the  $A_{\parallel}$  hyperfine features of  $\text{Cu}_2^\circ$ . Two equal  $A_{\parallel}$  values are required to fit the hyperfine pattern, reflecting an equal distribution of spin

**Table 1: g and A values obtained from fitting the X band EPR spectra of  $\text{Cu}_2^0$  and resting 1-hole  $\text{Cu}_2^*$  values from Ref. <sup>35</sup>.**

	$\text{Cu}_2^0$	$\text{Cu}_2^*$
$g_{\parallel}$	2.177	2.160
$A_{\parallel}$	$42 \times 10^{-4} \text{ cm}^{-1}$ $42 \times 10^{-4} \text{ cm}^{-1}$	$61 \times 10^{-4} \text{ cm}^{-1}$ $23 \times 10^{-4} \text{ cm}^{-1}$
$g_{\perp}$	$\sim 2.03$	2.042

over two coppers, while in resting  $\text{Cu}_2^*$  two unequal  $A_{\parallel}$  values are required, reflecting a spin distribution over two coppers of  $\sim 5:2$  in the resting state.<sup>35</sup> This indicates that the unpaired spin in the  $\text{Cu}_2^0$  intermediate has shifted from being mostly localized on  $\text{Cu}_I$ , as in resting 1-hole  $\text{Cu}_2^*$ , to being more equally delocalized over two different coppers.

**3.1.2 Absorption and MCD:** The absorption spectrum of  $\text{Cu}_2^0$ , obtained after the subtraction of the contributions of oxidized  $\text{Cu}_A$  and 1-hole  $\text{Cu}_Z$ , shows an asymmetrically shaped intense peak maximum at  $\sim 14,900 \text{ cm}^{-1}$  ( $\epsilon \approx 2000 \text{ M}^{-1} \text{ cm}^{-1}$ , Figure 3A) with a shoulder to higher energy. This absorption maximum is lower in energy by  $\sim 700 \text{ cm}^{-1}$  than that of resting 1-hole  $\text{Cu}_2^*$  (shown for comparison in Figure 3B). The absorption maximum correlates to a derivative shaped pseudo-A feature in the MCD spectrum of  $\text{Cu}_2^0$  comprised of a negative band at  $14,200 \text{ cm}^{-1}$  and a positive band at  $15,900 \text{ cm}^{-1}$  (Figure 3A, bands 5 and 6 respectively, band numbers taken from the fit of resting 1-hole  $\text{Cu}_2^*$  in Ref. <sup>20</sup>). Simultaneous fitting of the absorption and MCD spectra of  $\text{Cu}_2^0$  yields 6 transitions that can be clearly identified, which are assigned as d-d (band 3),  $\mu_4\text{S}^{2-}$  to Cu charge transfer (CT,

bands 5, 6 and 7), and His to Cu CT transitions (bands 9-10) based on their energies and  $C_0/D_0$  ratios following Ref. <sup>20</sup> (Table S1). The transitions that contribute to the absorption maximum and pseudo-A feature are  $\mu_4\text{S}^{2-}$  to Cu CT transitions that occur at very similar energies to the equivalent transitions (5 and 6) in resting 1-hole  $\text{Cu}_2^*$  (Table S1). Thus, while the absorption maximum of  $\text{Cu}_2^0$  appears to be at lower energy than in resting 1-hole  $\text{Cu}_2^*$ , this is due to a change in the *relative intensities* of the  $\mu_4\text{S}^{2-}$  to Cu CT transitions, not a shift in their energies. A recent study of the intensities of the  $\mu_4\text{S}^{2-}$  to Cu CT transitions in resting 1-hole  $\text{Cu}_2^*$  and 1-hole  $\text{Cu}_4\text{S}_2\text{Cu}_2$  has shown that these intensities reflect the overlap of the three perpendicular S p orbitals with the  $\beta$  LUMO of the cluster (Figure S3), such that a higher intensity for band 5 reflects more spin delocalization onto  $\text{Cu}_{IV}$  in the  $\beta$  LUMO while band 6 reflects the spin on  $\text{Cu}_I$ .<sup>36</sup> Thus, the change in relative intensities of the  $\mu_4\text{S}^{2-}$  to Cu CT transitions in  $\text{Cu}_2^0$  relative to resting 1-hole  $\text{Cu}_2^*$ , where band 6 decreases in intensity while band 5 increases, indicates that there is less spin on  $\text{Cu}_I$  and more spin on  $\text{Cu}_{IV}$  in the  $\text{Cu}_2^0$  intermediate. This confirms and provides insight into the observation from the EPR  $A_{\parallel}$  values that the spin density of the  $\text{Cu}_2^0$  intermediate cluster has shifted from being distributed  $\sim 5:2$  on  $\text{Cu}_I$  and  $\text{Cu}_{IV}$  in resting 1-hole  $\text{Cu}_2^*$  to being more delocalized to a second Cu (from MCD,  $\text{Cu}_{IV}$ ) in  $\text{Cu}_2^0$ . A direct way to accomplish this shift in spin density is to change the nature or position of the  $\text{Cu}_I$ - $\text{Cu}_{IV}$  edge ligand in the  $\text{Cu}_2^0$  relative to the  $\mu_2\text{OH}$  ligand in resting 1-hole  $\text{Cu}_2^*$ , such that the ligand field on  $\text{Cu}_I$  is decreased and the ligand field on  $\text{Cu}_{IV}$  is increased, leading to a shift of some of the spin density from  $\text{Cu}_I$  onto  $\text{Cu}_{IV}$ .

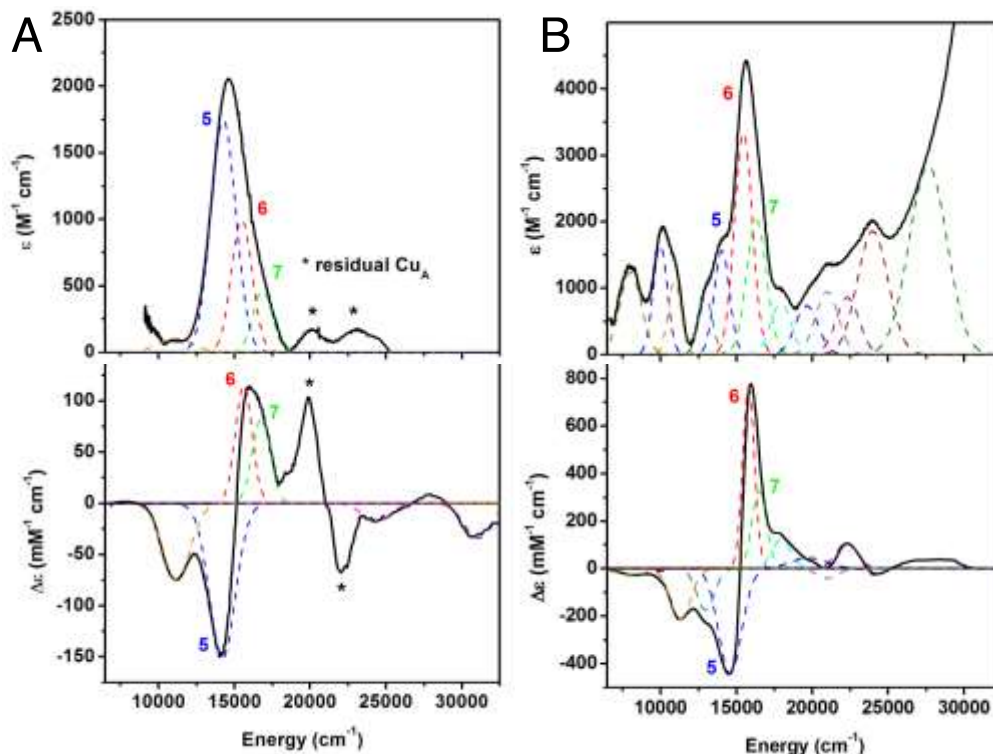


Figure 3: Absorption and MCD spectra of A)  $\text{Cu}_2^0$ , absorption at 273 K and MCD at 5 K and 7 T, and B) resting  $\text{Cu}_2^*$ , absorption at 5 K and MCD at 5 K, 7 T, showing the Gaussian bands obtained from a simultaneous fit, following the fit for  $\text{Cu}_2^*$  from Ref. <sup>17</sup>.

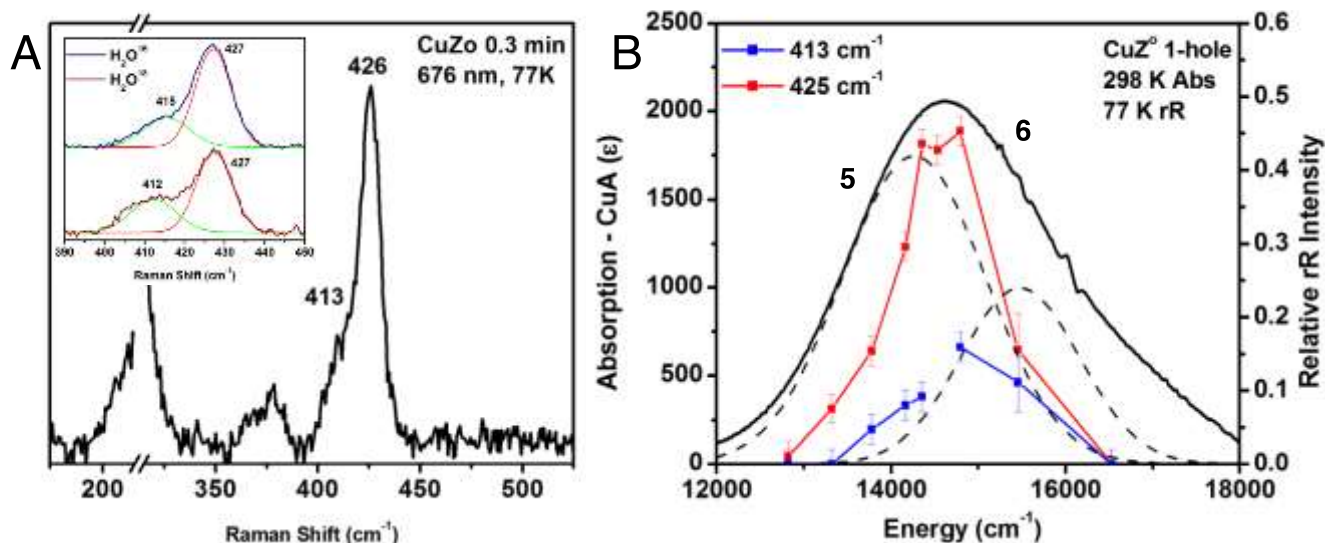


Figure 4: Resonance Raman spectrum and profile of  $\text{Cu}_2\text{O}$ , obtained after 15 s of reaction with  $\text{N}_2\text{O}$ . A) Spectrum at 77 K, excitation energy 676 nm. Inset:  $\text{O}^{16}/\text{O}^{18}$  isotope perturbation observed after formation of  $\text{Cu}_2\text{O}$  in  $\text{H}_2\text{O}^{16}$  or  $\text{H}_2\text{O}^{18}$  100 mM phosphate at pH 7.6. The  $\text{O}^{16}/\text{O}^{18}$  isotope data were fit with two bands of identical width, where in the  $\text{O}^{18}$  spectrum green band decreases in energy by  $3\text{ cm}^{-1}$  and has 36% more intensity. B) Left scale: Room temperature absorption of  $\text{Cu}_2\text{O}$  at 30 s (after subtraction of oxidized  $\text{Cu}_A$  and 1-hole  $\text{Cu}_Z$  contributions). Right scale: Dependence of the normalized intensity of the vibrations of  $\text{Cu}_2\text{O}$  on excitation energy.

**3.1.3 Resonance Raman:** Upon laser excitation into the absorption maximum of  $\text{Cu}_2\text{O}$ , two features are resonance enhanced in the Raman spectrum, an intense vibration at  $426\text{ cm}^{-1}$  and a weaker shoulder at  $413\text{ cm}^{-1}$  (Figure 4A). These vibrations profile in the most intense  $\mu_4\text{S}^{2-}$  to Cu CT transition (band 5), indicating that they are Cu-S stretching vibrations (Figure 4B). These Cu-S stretching vibrations occur at higher energy than those observed for resting 1-hole  $\text{Cu}_2^*$ , which has an intense Cu-S stretch at  $378\text{ cm}^{-1}$  and a weaker Cu-S stretch at  $362\text{ cm}^{-1}$  that profile similarly to the vibrations of  $\text{Cu}_2\text{O}$  (in band 6, the most intense S to Cu CT transition in  $\text{Cu}_2^*$ , Figure S4). This indicates that some of the Cu-S bonds are stronger in the  $\text{Cu}_2\text{O}$  intermediate relative to resting 1-hole  $\text{Cu}_2^*$ . Resting 1-hole  $\text{Cu}_2^*$  shows an additional Cu-S stretch at  $412\text{ cm}^{-1}$  that profiles differently (in the third sulfide to Cu CT transition, band 7), which is not observed in  $\text{Cu}_2\text{O}$  due to the low intensity of band 7 in  $\text{Cu}_2\text{O}$ . When the  $\text{Cu}_2\text{O}$  intermediate is formed in  $\text{H}_2\text{O}^{18}$  buffer, the  $413\text{ cm}^{-1}$  vibration shifts down in energy by  $3\text{ cm}^{-1}$  and increases in intensity by ~36%, while the  $426\text{ cm}^{-1}$  vibration remains unperturbed (Figure 4A, inset). Resting 1-hole  $\text{Cu}_2^*$  also shows some  $\text{H}_2\text{O}^{18}$  isotope sensitivity in the Cu-S stretch at  $412\text{ cm}^{-1}$  ( $-9\text{ cm}^{-1}$ ) but only at high pH. This  $\text{H}_2\text{O}^{18}$  sensitivity in resting 1-hole  $\text{Cu}_2^*$  has been previously assigned as coupling between a Cu-S core stretch and the Cu-O stretch of a hydroxide ligand that bridges the  $\text{Cu}_I$ - $\text{Cu}_{IV}$  edge.<sup>20</sup> The position of the edge hydroxide ligand is perturbed by the protonation state of Lys397, such that the edge ligand stretch only shows kinematic coupling to the core stretch at high pH (the hydroxide ligand is present in resting 1-hole  $\text{Cu}_2^*$  at both high and low pH).<sup>20</sup> The presence of a similar  $\text{H}_2\text{O}^{18}$  isotope shift in the  $413\text{ cm}^{-1}$  Cu-S stretch of the  $\text{Cu}_2\text{O}$  intermediate at neutral pH indicates that a solvent-exchangeable hydroxide edge ligand is also present in  $\text{Cu}_2\text{O}$ , since only the Cu-O stretches of a hydroxide will be high enough in energy to mix with the core Cu-S stretches of the cluster. The possibility of either a water

or a hydroxide solvent-derived edge ligand is computationally evaluated below, and only a hydroxide ligand predicts  $\text{H}_2\text{O}^{18}$  isotope sensitivity in a high energy Cu-S vibration. Thus, the presence of  $\text{H}_2\text{O}^{18}$  sensitivity in the  $413\text{ cm}^{-1}$  Cu-S core vibration indicates that the  $\text{Cu}_2\text{O}$  intermediate has a hydroxide ligand on the  $\text{Cu}_I$ - $\text{Cu}_{IV}$  edge, similar to resting 1-hole  $\text{Cu}_2^*$  but differing in the position of the edge ligand (from the change in spin density by EPR and MCD).

### 3.2 Kinetics.

**3.2.1 Reduction of  $\text{Cu}_2\text{O}$  versus 1-hole  $\text{Cu}_2^*$ :** It has been reported previously that  $\text{Cu}_2\text{O}$  is competent to be involved in rapid turnover, since the steady-state activity of  $Mh\text{N}_2\text{OR}$  decays at the same rate as the decay of the  $\text{Cu}_2\text{O}$  intermediate to resting 1-hole  $\text{Cu}_2^*$ .<sup>27</sup> This suggests that the reduction of  $\text{Cu}_2\text{O}$  under steady-state turnover conditions occurs with a rate equal to or faster than  $k_{\text{cat}}$  ( $320 \pm 20\text{ s}^{-1}$  for  $Mh\text{N}_2\text{OR}$ , used in this study).<sup>26</sup> However, the reductant used in these assays, dithionite-reduced methyl viologen, is not physiologically relevant. To resolve this issue, we investigated whether  $\text{Cu}_2\text{O}$  can be reduced by the milder, physiologically relevant reductant sodium ascorbate. The reduction of  $\text{Cu}_2\text{O}$  upon addition of sodium ascorbate could be confirmed by resonance Raman spectroscopy, which shows that several minutes after addition of sodium ascorbate the vibrations at  $426$  and  $413\text{ cm}^{-1}$  associated with  $\text{Cu}_2\text{O}$  disappear (Figure S5) indicating that, unlike resting 1-hole  $\text{Cu}_2^*$ , the  $\text{Cu}_2\text{O}$  intermediate can be reduced by sodium ascorbate.

For kinetic studies using absorption spectroscopy on a faster timescale,  $\text{Cu}_2\text{O}$  was formed *in situ* through the reaction of fully reduced  $\text{N}_2\text{OR}$  with close to stoichiometric  $\text{N}_2\text{O}$ , and a ~400-fold excess of sodium ascorbate was subsequently added (e.g., 7.3 mM sodium ascorbate, 20  $\mu\text{M}$   $Mh\text{N}_2\text{OR}$ ). Addition of sodium ascorbate to  $\text{Cu}_2\text{O}$  leads to rapid decay of both the absorption maximum of  $\text{Cu}_2\text{O}$  at  $14,900\text{ cm}^{-1}$  (Figure 5A and 5B, red) and the characteristic absorption features of

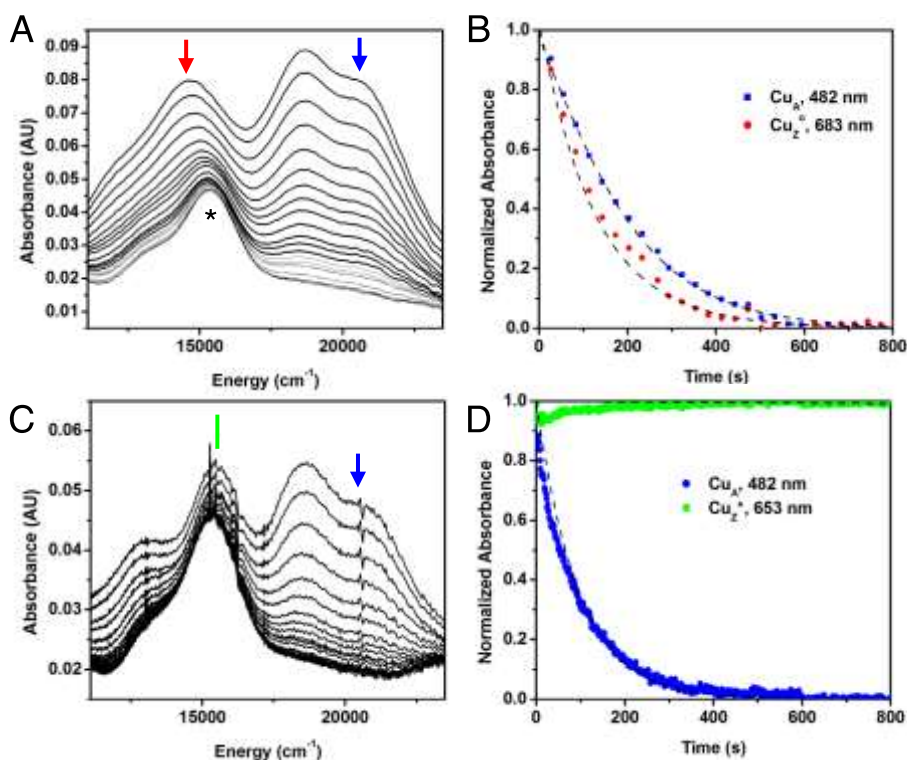


Figure 5: Sodium ascorbate reduction of  $\text{Cu}_2^\circ$  and resting 1-hole  $\text{Cu}_2^*$ . A) Absorption spectra of the reduction of  $\text{Cu}_2^\circ$  (red arrow) and oxidized  $\text{Cu}_A$  (blue arrow) by 7.3 mM (~400 equivalents) sodium ascorbate, added 37 seconds after the initial  $\text{N}_2\text{O}$  addition to form  $\text{Cu}_2^\circ$  *in situ* at 297 K. Spectra recorded every 0.5 minutes. \*Indicates resting 1-hole  $\text{Cu}_2^*$ , formed by  $\text{Cu}_2^\circ$  decay during the first 37 seconds before ascorbate addition. B) Normalized time dependence of the reduction of  $\text{Cu}_2^\circ$  at 683 nm (red) and oxidized  $\text{Cu}_A$  at 482 nm (blue). Kinetic fit using Scheme S2 given by dashed black lines. C) Absorption spectra of the reduction of resting  $\text{Cu}_2^*$  (green line) and oxidized  $\text{Cu}_A$  (blue arrow) by 5 mM (250 equivalents) sodium ascorbate at 297 K, spectra recorded every 1 minute. D) Normalized time dependence of the reduction of oxidized  $\text{Cu}_A$  at 482 nm (blue) and lack of reduction of resting 1-hole  $\text{Cu}_2^*$  at 653 nm (green). Kinetic fit using Scheme S1 given by dashed black lines.

oxidized  $\text{Cu}_A$  (20,800, 18,800, and 12,200  $\text{cm}^{-1}$ , Figure 5A and 5B, blue) in the first 800 seconds, with slightly faster reduction of  $\text{Cu}_2^\circ$  relative to  $\text{Cu}_A$  (Figure 5B). These data are consistent with either the rapid reduction of  $\text{Cu}_2^\circ$  via electron transfer from  $\text{Cu}_A$  or, less plausibly, rapid direct reduction of  $\text{Cu}_2^\circ$  by sodium ascorbate at a very similar rate to the sodium ascorbate reduction of  $\text{Cu}_A$  (despite differences between  $\text{Cu}_A$  and  $\text{Cu}_2^\circ$  in accessibility to the reductant). Thus, these data likely reflect reduction of  $\text{Cu}_2^\circ$  by sodium ascorbate via intramolecular electron transfer (IET) from  $\text{Cu}_A$ . This contrasts with the sodium ascorbate reduction of resting 1-hole  $\text{Cu}_2^*$ , where the absorption features of oxidized  $\text{Cu}_A$  (Figure 5C and 5D, blue) immediately decay but those of resting 1-hole  $\text{Cu}_2^*$  remain (Figure 5C and D, green). A kinetic model that includes two steps, the bimolecular reduction of  $\text{Cu}_A$  by sodium ascorbate ( $k_{\text{red}} = 1.4 \text{ M}^{-1} \text{ s}^{-1}$ ) and potential IET from reduced  $\text{Cu}_A$  to 1-hole  $\text{Cu}_2^*$  (Scheme S1), yields an upper limit for  $k_{\text{IET}}$  of  $1 \times 10^{-5} \text{ s}^{-1}$  for the unobserved reduction of 1-hole  $\text{Cu}_2^*$  by  $\text{Cu}_A$  (Figure 5D, dashed lines). A more extended kinetic model, which also accounts for the possibility of the decay of  $\text{Cu}_2^\circ$  to 1-hole  $\text{Cu}_2^*$  (Scheme S2), has been used to fit the reduction of  $\text{Cu}_A$  and  $\text{Cu}_2^\circ$  (Figure 5B, dashed lines). The data are well fitted by this model with a bimolecular rate of sodium ascorbate reduction of  $\text{Cu}_A$  of  $1.1 \text{ M}^{-1} \text{ s}^{-1}$ , similar to the value

observed for  $\text{Cu}_A$  reduction in the presence of 1-hole  $\text{Cu}_2^*$ , and a lower limit on  $k_{\text{IET}}$  of  $0.1 \text{ s}^{-1}$  for the possible reduction of  $\text{Cu}_2^\circ$  by  $\text{Cu}_A$  (Figure 5B, dashed lines). The best fit requires that the electron transfer step be reversible with a  $K_{\text{IET}}$  of 3.3, indicating that  $\text{Cu}_2^\circ$  and  $\text{Cu}_A$  have similar redox potentials. The reduction of  $\text{Cu}_2^\circ$  by  $\text{Cu}_A$  using a physiologically relevant reductant establishes that  $\text{Cu}_2^\circ$  can be the oxidized form of the enzyme that participates in turnover *in vivo*, while resting 1-hole  $\text{Cu}_2^*$ , which cannot be reduced by  $\text{Cu}_A$ , is an inactive state that does not participate in reactivity. The rate of conversion of  $\text{Cu}_2^\circ$  to resting 1-hole  $\text{Cu}_2^*$ , previously established from the decay of enzymatic activity, is  $\sim 5 \times 10^{-3} \text{ s}^{-1}$ ,<sup>27</sup> two orders of magnitude slower than the lower limit for IET from  $\text{Cu}_A$  to  $\text{Cu}_2^\circ$ . Additionally, the rate of  $\text{Cu}_A$  reduction of  $\text{Cu}_2^\circ$  is at least  $10^4$  faster than the reduction of 1-hole  $\text{Cu}_2^*$  by  $\text{Cu}_A$ . The origin of this difference in electron transfer rates will be considered below.

Note that the above analysis of reduction of  $\text{Cu}_A$  and  $\text{Cu}_2^\circ$  together by sodium ascorbate reflect experimental results up to 800 seconds, at which point complete reduction of  $\text{Cu}_A$  and  $\text{Cu}_2^\circ$  is observed. After 800 seconds, a second phase of reactivity is observed, in which there is slow growth of an absorption feature at 16,000  $\text{cm}^{-1}$  (Figure S6A). This is consistent with a slow one electron oxidation of the fully reduced

$\text{Cu}_4\text{S}$  cluster to resting 1-hole  $\text{Cu}_2^*$ . No comparable growth at  $16,000\text{ cm}^{-1}$  (i.e., oxidation to form resting 1-hole  $\text{Cu}_2^*$ ) is observed during turnover of  $MhN_2OR$  with ascorbate, performed by premixing fully reduced  $MhN_2OR$  and ascorbate before addition of  $\text{N}_2\text{O}$  (Figure S6B). This indicates that the slow one electron oxidation of the  $\text{Cu}_4\text{S}$  cluster observed after reduction of  $\text{Cu}_2^0$  and  $\text{Cu}_A$  by sodium ascorbate (Figure S6A) is a side reaction that is not relevant to turnover.

**3.2.2 Steady-state kinetics:** The steady-state turnover of  $MhN_2OR$  was studied at different temperatures to obtain thermodynamic parameters for the rate-determining step. The initial rate of oxidation of methyl viologen was used to obtain a plot of  $\ln(k)$  vs  $1/T$  (Figure 6A) that was fit to the Arrhenius equation using a linear regression analysis to obtain a  $\Delta E_A$  of  $10 \pm 2\text{ kcal/mol}$ . Similarly,  $\ln(k/T)$  vs  $1/T$  was plotted (Figure 6B) and fit to the Eyring equation to obtain a  $\Delta H^\ddagger$  of  $10 \pm 1\text{ kcal/mol}$  and  $\Delta S^\ddagger$  of  $-13 \pm 1\text{ cal mol}^{-1}\text{ K}^{-1}$ . This yields a  $\Delta G^\ddagger$  at room temperature of  $13 \pm 2\text{ kcal/mol}$ , consistent with the  $\Delta G^\ddagger$  predicted based on the  $k_{cat}$  of  $MhN_2OR$  ( $k_{cat} = 320\text{ s}^{-1}$  at  $293\text{ K}$ , corresponding to a  $\Delta G^\ddagger$  of  $13\text{ kcal/mol}$ ). The small value obtained for  $\Delta S^\ddagger$  indicates that the rate-limiting step of turnover does not involve either binding of  $\text{N}_2\text{O}$  or loss of  $\text{N}_2$ . The specific activity  $MhN_2OR$  shows a bell-shaped dependence on pH and pD (Figure 7). The enzyme attains optimum activity at pH  $\sim 8$  and loses activity at lower and higher pH

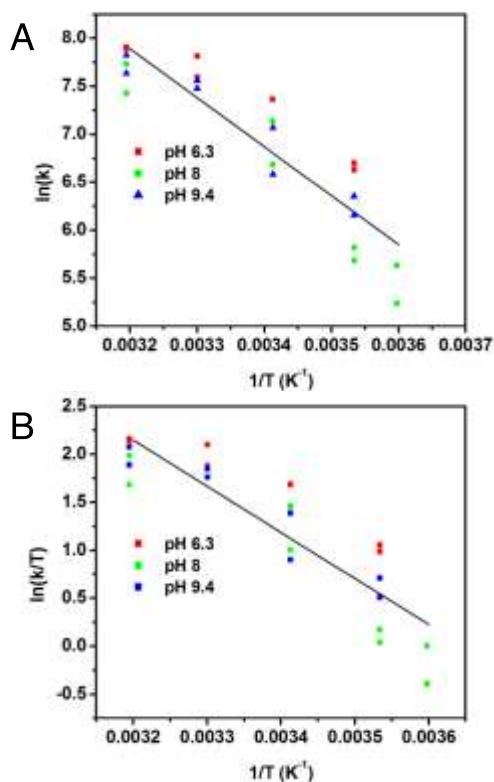


Figure 6: Temperature dependence of the initial rate of methyl viologen consumption during steady-state turnover of  $\text{N}_2\text{OR}$ . A) Arrhenius plot, with linear fit ( $R^2 = 0.8298$ ). B) Eyring plot, with linear fit ( $R^2 = 0.8119$ ). Colors indicate temperature dependence data at different pH values: pH 6.3 (red), pH 8.0 (green) and pH 9.4 (blue).

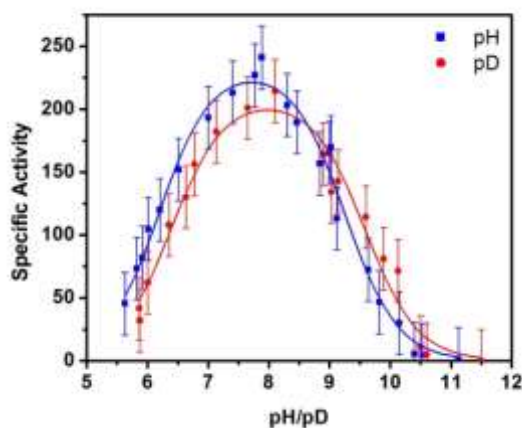


Figure 7: The pH and pD profiles of steady-state activity of  $MhN_2OR$  at  $297\text{ K}$  in  $\mu\text{mol N}_2\text{O min}^{-1}\text{ mg}^{-1}$ , fit with a speciation curve generated by  $\text{pKa(H)}$  values of  $6.19 \pm 0.05$  and  $9.15 \pm 0.05$  (blue) and  $\text{pKa(D)}$  values of  $6.4 \pm 0.1$  and  $9.5 \pm 0.1$ , with a solvent deuterium isotope effect of  $1.12 \pm 0.06$  (red).

with  $\text{pKa}$  values of  $6.19 \pm 0.05$  and  $9.15 \pm 0.05$ . The lower value is consistent with the  $\text{pKa}$  determined in a previous study of the intermolecular rate constant between  $MhN_2OR$  and reduced methyl viologen.<sup>26</sup> The  $\text{pKa}$  values are shifted by 0.2 and 0.3 log units, respectively, when the steady-state turnover experiments are performed in deuterated buffer. A small solvent kinetic isotope effect (SKIE) of  $1.12 \pm 0.06$  is observed at optimum pH, indicating that a solvent exchangeable proton contributes to the transition state in the rate determining step but is not significantly transferred. The temperature dependence of the initial rate of  $\text{N}_2\text{O}$  reduction shows no significant variation outside of error when performed at three different pH values (Figure 6), indicating that the same species is responsible for activity at all pH's. Thus, the bell-shaped pH profile of activity reflects protonation equilibria between three species, where only the species present at intermediate pH is active. The inactive high pH species can be assigned as having Lys397 deprotonated, since the  $\text{pKa}$  of 9.15 determined for loss of activity at high pH is identical to that determined for Lys397 based on the pH dependence of the spectral features of resting 1-hole  $\text{Cu}_2^*$  and its reduction.<sup>20</sup> The  $\text{pKa}$  value of 6.19 corresponds to that expected for the second protonation of a His sidechain but no changes in the absorption features of oxidized  $\text{Cu}_A$  or resting 1-hole  $\text{Cu}_2^*$  are observed between pH 7.6 and pH 5 (Figure S7), indicating that the protonation does not occur at one of the copper sites in the resting state. It is possible that the residue being protonated affects the conformation of the protein or that the  $\text{pKa}$  is associated with a His in some reduced state in turnover (e.g. reduced  $\text{Cu}_A$  or the fully reduced  $\text{Cu}_4\text{S}$  cluster).

### 3.3 Calculations.

#### 3.3.1 Model of $\text{Cu}_2^0$ relative to $\text{Cu}_2^*$ : spectral assignments.

DFT calculations were performed to assess possible structural models for the  $\text{Cu}_2^0$  intermediate and evaluate their correlation to the spectroscopic features observed experimentally.



A viable model for  $\text{Cu}_2^\circ$  must reproduce the observed shift of the unpaired spin density from dominantly on  $\text{Cu}_I$  in resting 1-hole  $\text{Cu}_2^*$  to more on  $\text{Cu}_{IV}$ , the shift in the Cu-S vibrations of the cluster to higher energy, and the presence of a solvent  $\text{O}^{18}$  isotope effect on a Cu-S vibration (indicating the presence of a solvent derived edge ligand). Possible models for  $\text{Cu}_2^\circ$  were obtained by evaluating chemically reasonable perturbations to a spectroscopically calibrated model of resting 1-hole  $\text{Cu}_2^*$  (with protonated Lys397). Resting 1-hole  $\text{Cu}_2^*$  was modeled well with a hydroxide ligand asymmetrically bridging the  $\text{Cu}_I$ - $\text{Cu}_{IV}$  edge, closer to  $\text{Cu}_I$  than  $\text{Cu}_{IV}$  (2.00 and 2.09 Å, Figure 8A). The model includes two second

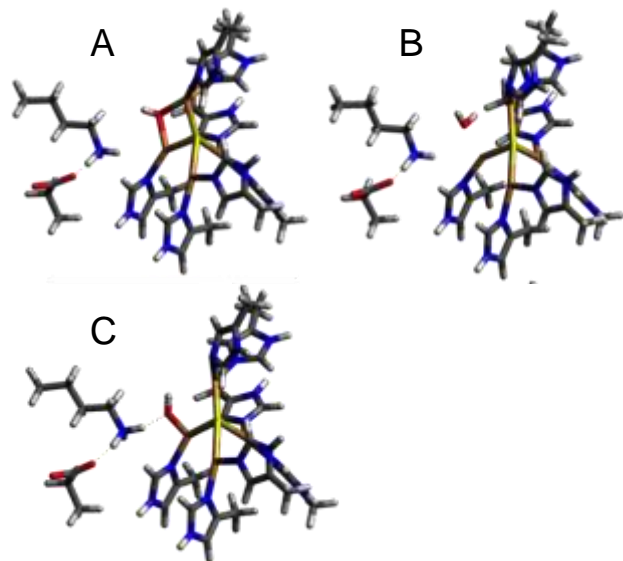


Figure 8: Optimized structures of 1-hole  $\text{Cu}_4\text{S}$  models with different edge ligation. A) Hydroxide bridged model for resting 1-hole  $\text{Cu}_2^*$ , B) water edge ligand, and C) hydroxide coordinated terminally to  $\text{Cu}_{IV}$  and hydrogen bonded to Lys397. B) and C) are assessed as possible models for the  $\text{Cu}_2^\circ$  intermediate. (B<sub>3</sub>LYP, tzvp on  $\text{Cu}_4\text{SON}_7$ ,  $\text{NH}_3^+$  and  $\text{CO}_2^-$ , sv on remainder, PCM=10).

sphere residues, Lys397 and Glu435, that are hydrogen-bonded to each other and near to  $\text{Cu}_{IV}$ , such that Lys397 is 4.02 Å from the  $\mu_2\text{OH}$ . This is extended from our previous computational model, which only included Lys397.<sup>20</sup> When Lys397 in the previous model was protonated, it moves significantly from its crystallographic position to hydrogen bond to the edge hydroxide, which then coordinates directly to  $\text{Cu}_I$  instead of bridging  $\text{Cu}_I$  and  $\text{Cu}_{IV}$ .<sup>20</sup> The present model reproduces the previously observed spectroscopic data for resting 1-hole  $\text{Cu}_2^*$ , including the minimal perturbation at high pH when Lys397 is deprotonated,<sup>20</sup> without requiring Lys397 to move from its crystallographically defined position (see Supporting).

First, possible models of  $\text{Cu}_2^\circ$  resulting from protonation or deprotonation of the edge hydroxide in resting 1-hole  $\text{Cu}_2^*$  were considered. Protonation results in a model with a water ligand on the  $\text{Cu}_I$ - $\text{Cu}_{IV}$  edge, closer to  $\text{Cu}_{IV}$  than  $\text{Cu}_I$  (Figure 8B), while deprotonation to form a bridging oxo leads to proton transfer from Lys397 and results in a  $\mu_2\text{OH}$  and deprotonated Lys. The latter is the same model as was developed

in Ref.<sup>20</sup> for the high pH form of resting 1-hole  $\text{Cu}_2^*$ , which is not active in turnover, and excluded as a model for  $\text{Cu}_2^\circ$ . In the protonated model, the water binds weakly on the  $\text{Cu}_I$ - $\text{Cu}_{IV}$  edge, 2.26 Å from  $\text{Cu}_{IV}$  and 3.39 Å from  $\text{Cu}_I$ . Lys397 remains close to its crystallographic position and does not interact with the water edge ligand (Table S2). An additional model was evaluated resulting from a perturbation of the position of the hydroxide ligand on the  $\text{Cu}_I$ - $\text{Cu}_{IV}$  edge. By positioning the hydroxide ligand near  $\text{Cu}_{IV}$  and protonated Lys397, a structure was obtained with a terminal hydroxide ligand coordinated to  $\text{Cu}_{IV}$  (Cu-O bond length of 1.93 Å) and directly hydrogen bonded to Lys397, which remains in its crystallographic position and hydrogen bonded to Glu435 (Figure 8C). The effects of these perturbations on the calculated spin distribution and vibrations were used to determine which of these models is consistent with the spectral features of  $\text{Cu}_2^\circ$  relative to those of resting 1-hole  $\text{Cu}_2^*$ .

The calculated Mulliken atomic spin density for the  $\text{OH}_2$  model and the  $\text{Cu}_{IV}$ -OH model, relative to our  $\text{OH}^-$  bridged model for resting 1-hole  $\text{Cu}_2^*$ , are given in Table 2. In the  $\text{OH}_2$

**Table 2: Mulliken atomic spin density distribution for computational 1-hole  $\text{Cu}_4\text{S}$  models with different  $\text{Cu}_I$ - $\text{Cu}_{IV}$  edge ligation, given in Figure 8 (B<sub>3</sub>LYP, tzvp on  $\text{Cu}_4\text{SON}_7$ ,  $\text{NH}_3^+$  and  $\text{CO}_2^-$ , sv on remainder, PCM=10).**

Edge Ligand	Mulliken Atomic Spin Density					
	$\text{Cu}_I$	$\text{Cu}_{II}$	$\text{Cu}_{III}$	$\text{Cu}_{IV}$	$\text{S}^{2-}$	O
$\text{OH}^-$ bridge	0.26	0.12	0.07	0.12	0.26	0.08
$\text{OH}_2$	0.08	0.26	0.13	0.12	0.24	0.00
$\text{Cu}_{IV}$ -OH	0.07	0.15	0.03	0.32	0.21	0.10

model, the spin density decreases on  $\text{Cu}_I$  (from 26% to 8%) and increases on  $\text{Cu}_{II}$  (12% to 26%), while the spin on  $\text{Cu}_{IV}$  remains constant. The  $\text{Cu}_{IV}$ -OH model shows a similar decrease in spin density on  $\text{Cu}_I$  (26% to 7%) and a three-fold increase in spin density on  $\text{Cu}_{IV}$  (12% to 32%), with no significant change on  $\text{Cu}_{II}$ . Thus, only the  $\text{Cu}_{IV}$ -OH model reproduced the shift in spin density from  $\text{Cu}_I$  to  $\text{Cu}_{IV}$  observed in the absorption and MCD spectra. In this model the unpaired spin is delocalized ~2:1 over  $\text{Cu}_{IV}$  and  $\text{Cu}_{II}$ . This is more localized than is observed for the  $\text{Cu}_2^\circ$  intermediate experimentally based on the EPR hyperfine values, which indicate a 1:1 distribution of spin over two coppers. This suggests that the  $\text{Cu}_{IV}$ -OH model, while reproducing the spin density shift, overestimates the strength of the ligand field on  $\text{Cu}_{IV}$ . This effect could arise from the hydrogen bond from Lys397 to the hydroxide being weaker in the model than in the protein, leading to a stronger hydroxide- $\text{Cu}_{IV}$  interaction. This would result from an overly strong interaction between the negatively charged Glu435 and the Lys, since there are other hydrogen bonding interactions with Glu435 present in the crystal structure (from a backbone amide and a localized water molecule) that are not included in the computational model.

Experimentally, the  $\text{Cu}_2^\circ$  intermediate is characterized by two vibrations at 426 and 413  $\text{cm}^{-1}$  (split by 13  $\text{cm}^{-1}$ ) where the

lower energy vibration shows a  $-3\text{ cm}^{-1}$  solvent  $\text{O}^{18}$  isotope shift. The highest energy Cu-S stretch in  $\text{Cu}_2^\circ$  is shifted up in energy by  $47\text{ cm}^{-1}$  relative to resting 1-hole  $\text{Cu}_2^*$ . The energies of the predicted Cu-S and Cu-OH/ $\text{OH}_2$  vibrations for the possible models of  $\text{Cu}_2^\circ$  compared to the resting 1-hole  $\text{Cu}_2^*$  model are given in Table S3. In the resting 1-hole  $\text{Cu}_2^*$  model, the highest energy core Cu-S vibration occurs at  $340\text{ cm}^{-1}$  ( $378\text{ cm}^{-1}$  experimentally) and has dominant  $\text{Cu}_{\text{II}}-\mu_4\text{S}$  and  $\text{Cu}_{\text{IV}}-\mu_4\text{S}$  stretching character. In both possible models for  $\text{Cu}_2^\circ$ , this vibration shifts up in energy due to a significant decrease in the  $\text{Cu}_{\text{IV}}-\mu_4\text{S}$  bond length (from  $2.25\text{ \AA}$  to  $2.19\text{ \AA}$  in both models). For the  $\text{OH}_2$  model, a localized  $\text{Cu}_{\text{IV}}-\text{S}$  stretch is predicted at  $392\text{ cm}^{-1}$ , while in the  $\text{Cu}_{\text{IV}}-\text{OH}$  model this vibration occurs at  $386\text{ cm}^{-1}$  ( $52$  and  $44\text{ cm}^{-1}$  higher in energy than the  $\text{Cu}_{\text{IV}}-\text{S}$  vibration of resting 1-hole  $\text{Cu}_2^*$ , respectively). While both models predict the increased energy of Cu-S vibrations with  $\text{Cu}_{\text{IV}}-\text{S}$  stretching character, only the  $\text{Cu}_{\text{IV}}-\text{OH}$  model is consistent with the solvent  $\text{O}^{18}$  isotope shift present in the  $\text{Cu}_2^\circ$  intermediate. In the  $\text{OH}_2$  model the  $\text{Cu}_{\text{IV}}-\text{S}$  stretch shows no predicted shift with  $\text{O}^{18}$ , while a  $-2\text{ cm}^{-1}$  shift is predicted in the  $\text{Cu}_{\text{IV}}-\text{OH}$  model. This difference results from greater mixing between the  $\text{Cu}_{\text{IV}}-\text{S}$  and  $\text{Cu}_{\text{IV}}-\text{OH}$  modes in the  $\text{Cu}_{\text{IV}}-\text{OH}$  model because the  $\text{Cu}_{\text{IV}}-\text{OH}$  stretch is higher in energy and thus closer in energy to the  $\text{Cu}_{\text{IV}}-\text{S}$  stretch ( $\text{Cu}_{\text{IV}}-\text{O}$  of  $467\text{ cm}^{-1}$  in the  $\text{Cu}_{\text{IV}}-\text{OH}$  model and  $202\text{ cm}^{-1}$  in the  $\text{OH}_2$  model, both with  $\text{O}^{18}$  shifts of  $-16\text{ cm}^{-1}$ ). This reflects the shorter  $\text{Cu}_{\text{IV}}-\text{OH}$  bond relative to the  $\text{Cu}_{\text{IV}}-\text{OH}_2$  bond ( $1.93\text{ \AA}$  versus  $2.26\text{ \AA}$ ).

Thus, the correlations of the predicted spin density distribution and vibrations of  $\text{OH}_2$  and  $\text{Cu}_{\text{IV}}-\text{OH}$  models with the spectral features of  $\text{Cu}_2^\circ$  support modeling  $\text{Cu}_2^\circ$  as an intermediate with a terminal hydroxide ligand coordinated to  $\text{Cu}_{\text{IV}}$  and hydrogen bonding to a protonated Lys397. This is consistent with the experimental pKa of Lys397 in resting 1-hole  $\text{Cu}_2^*$  of 9.2, which would only be increased by an additional hydrogen bond to the hydroxide in the  $\text{Cu}_{\text{IV}}-\text{OH}$  model, indicating that at the pH of 7.6, used for the spectroscopy of  $\text{Cu}_2^\circ$ , Lys397 will be protonated. While the  $\text{Cu}_{\text{IV}}-\text{OH}$  structure is at a local minimum with all real vibrational frequencies (aside from those resulting from the fixed atoms that model the connections to the protein backbone), this  $\text{Cu}_2^\circ$  model is  $6.4\text{ kcal/mol}$  higher in free energy than the OH bridged model of resting 1-hole  $\text{Cu}_2^*$ . Thus, the  $\text{Cu}_2^\circ$  intermediate is a metastable 1-hole form of the cluster formed as the kinetic product of turnover, which decays to the thermodynamically favored resting 1-hole form of  $\text{Cu}_2^*$ . The rate of decay of  $\text{Cu}_2^\circ$  to resting 1-hole  $\text{Cu}_2^*$  observed experimentally is  $5 \times 10^{-3}\text{ s}^{-1}$ , which gives a  $\Delta G^\ddagger$  of  $\sim 20\text{ kcal/mol}$ . We calculate a transition state with a  $\Delta G^\ddagger$  of  $6\text{ kcal/mol}$  (Figure S8) for breaking the hydrogen bond between Lys397 and the  $\text{Cu}_{\text{IV}}-\text{OH}$  to form the hydroxide bridge interacting with  $\text{Cu}_{\text{I}}$  (with a constrained  $\text{Cu}_{\text{I}}-\text{Cu}_{\text{IV}}$  distance). We expect this to be a lower limit as the hydrogen bond in this model appears to be weak relative to experiment, due to an overly strong interaction between Lys397 and Glu435 (see above).

**3.3.2 Rapid reduction of  $\text{Cu}_2^\circ$  for catalysis:** The sodium ascorbate reduction kinetic results presented above demon-

strate that  $\text{Cu}_2^\circ$  is rapidly reduced, likely by intramolecular electron transfer from  $\text{Cu}_A$ , while resting 1-hole  $\text{Cu}_2^*$  is not, with at least a  $10^4$ -fold greater  $k_{\text{IET}}$  to  $\text{Cu}_2^\circ$  relative to resting 1-hole  $\text{Cu}_2^*$ . Using the spectroscopically calibrated models for the  $\text{Cu}_2^\circ$  intermediate and resting  $\text{Cu}_2^*$  in Figures 8C and 8A, respectively, it is possible to explore the origin of this difference in intramolecular electron transfer rates, which is the basis for the functional role of  $\text{Cu}_2^\circ$  in turnover. Our computational results indicate that resting 1-hole  $\text{Cu}_2^\circ$  is metastable and  $+6.4\text{ kcal/mol}$  higher in energy than resting 1-hole  $\text{Cu}_2^*$ , resulting in an increased driving force for the IET, compared to resting 1-hole  $\text{Cu}_2^*$ . Three parameters in Marcus Theory<sup>37</sup> determine the rate of electron transfer: the free energy difference, which provides the driving force for the electron transfer ( $\Delta G^\circ$ ); the reorganization energy,  $\lambda$  (the sum of inner sphere,  $\lambda_i$  (i.e. bond changes), and outer sphere,  $\lambda_o$  (i.e. solvation changes)); and the electronic coupling between the donor and acceptor sites in the electron transfer process, given by the matrix element  $H_{\text{DA}}$ . To evaluate whether the  $\Delta\Delta G^\circ$  of  $+6.4\text{ kcal/mol}$  is sufficient to account for the  $>10^4$ -fold faster electron transfer rate observed experimentally, we determined a value for  $\lambda_i$  using our computational models of  $\text{Cu}_2^\circ$  and resting  $\text{Cu}_2^*$ . The inner sphere reorganization energy is given by  $\frac{1}{2}[E_{\text{ox}}(\text{red geom}) - E_{\text{ox}}(\text{ox geom}) + E_{\text{red}}(\text{ox geom}) - E_{\text{red}}(\text{red geom})]$ . The reduction of 1-hole  $\text{Cu}_2^\circ$  to fully reduced  $\text{Cu}_4\text{S}$  and water is a proton-coupled electron transfer (PCET) process. For a concerted PCET process, following Refs <sup>38</sup> and <sup>39</sup>,  $E_{\text{ox}}(\text{red geom})$  is obtained by calculating the oxidized energy at a reduced geometry without the additional proton, and  $E_{\text{red}}(\text{ox geom})$  is obtained by calculating the reduced energy at an oxidized geometry with the addition of the proton. These calculations yield  $\lambda_i$  values of  $0.32\text{ eV}$  for  $\text{Cu}_2^\circ$  and  $0.37\text{ eV}$  for resting 1-hole  $\text{Cu}_2^*$ . These values seem low relative to the inner sphere reorganization energies observed for other multinuclear copper sites (e.g.  $\lambda_i = 1.1\text{ eV}$  for the one electron reduction of the  $3\text{Cu}^{\text{II}}$  NI intermediate in the multicopper oxidases).<sup>40</sup> However, in  $\text{Cu}_2^\circ$  and  $\text{Cu}_2^*$  the nuclear reorganization is distributed over four coppers, with spin dominantly on two, which may contribute to the lower calculated inner sphere reorganization energy.<sup>41</sup> To ensure that the effect of  $\Delta\Delta G^\circ$  on  $\Delta k_{\text{IET}}$  is chemically reasonable, a range of  $\lambda_i$  values from  $0.4$ - $1.1\text{ eV}$  was evaluated. Together with a reasonable value for  $\lambda_o$  for  $\text{Cu}_2^\circ$  ( $0.24\text{ eV}$ ) and the experimentally determined  $\lambda_{\text{total}}$  for  $\text{Cu}_A$  ( $0.4\text{ eV}$ ) these yield a  $\lambda_{\text{total}}$  range of  $0.32$ - $1\text{ eV}$  for electron transfer from  $\text{Cu}_A$  to  $\text{Cu}_2^\circ$  or resting 1-hole  $\text{Cu}_2^*$  (see Supporting). Since there is no experimental value for  $H_{\text{DA}}$  for electron transfer from  $\text{Cu}_A$  to  $\text{Cu}_2^\circ$ , a wide range of possible values ( $0.001$ - $0.5\text{ cm}^{-1}$ ) was considered based on estimates for related sites (see Supporting). Using these values, we calculate a range of  $\Delta\Delta G^\circ$  values in the limit where  $H_{\text{DA}}$  and  $\lambda$  for ET from  $\text{Cu}_A$  to  $\text{Cu}_2^\circ$  and from  $\text{Cu}_A$  to resting 1-hole  $\text{Cu}_2^*$  are equal. Given the above ranges of  $\lambda_{\text{total}}$  and  $H_{\text{DA}}$  values, a  $\Delta\Delta G^\circ$  of  $5$ - $10\text{ kcal/mol}$  is sufficient to produce a  $10^4$ -fold faster electron transfer rate from  $\text{Cu}_A$  to  $\text{Cu}_2^\circ$ , which is consistent with the calculated  $\Delta G$  of  $+6.4\text{ kcal/mol}$  of  $\text{Cu}_2^\circ$  relative to resting 1-hole  $\text{Cu}_2^*$ . Thus, the origin of the  $>10^4$ -fold increase in the rate of electron transfer

from  $\text{Cu}_A$  to  $\text{Cu}_Z^0$  relative to resting 1-hole  $\text{Cu}_Z^*$  is thermodynamic, and the role of the hydrogen-bonded second sphere Lys397 is to stabilize the metastable  $\text{Cu}_Z^0$  intermediate to provide the driving force required for rapid reduction of the 1-hole oxidized state during catalysis.

**3.3.3 Reaction Coordinate for N-O Bond Cleavage:** Previous computational studies of the reaction mechanism of  $\text{N}_2\text{OR}$ , starting with  $\text{N}_2\text{O}$  binding to the fully reduced cluster, have predicted a 2-hole intermediate with a  $\mu_2$ -oxo or hydroxo ligand bridging the  $\text{Cu}_I$ - $\text{Cu}_{IV}$  edge as the product of the N-O bond cleavage step.<sup>8,34</sup> However, upon subsequent protonation and reduction, these species yield inactive resting 1-hole  $\text{Cu}_Z^*$  (i.e., a 1-hole cluster with a  $\mu_2$ -hydroxo edge ligand), rather than the reactive 1-hole  $\text{Cu}_{IV}$ -OH  $\text{Cu}_Z^0$  intermediate identified above. Using the experimentally validated computational models of 1-hole  $\text{Cu}_Z^0$  and resting 1-hole  $\text{Cu}_Z^*$  from Section 3.3.1, we have explored the reaction coordinate for N-O bond cleavage, and subsequent protonation and reduction, to determine how a 1-hole  $\text{Cu}_{IV}$ -OH intermediate (i.e.  $\text{Cu}_Z^0$ ) can arise from N-O bond cleavage.

$\text{N}_2\text{O}$  coordination to the fully reduced cluster results in a linear  $\text{N}_2\text{O}$  molecule terminally N-coordinated to  $\text{Cu}_I$ . However, upon N-O bond elongation by 0.1-0.2 Å to start the N-O bond cleavage reaction, the structure rearranges to form a  $\mu_{-1,3}$  coordination geometry, with the O of  $\text{N}_2\text{O}$  coordinating to  $\text{Cu}_{IV}$  and hydrogen-bonded to Lys397. This suggests that the N-O bond cleavage reaction proceeds via the  $\mu_{-1,3}$  isomer. To be able to study a system with a stable  $\mu_{-1,3}$   $\text{N}_2\text{O}$  isomer, we performed additional calculations on the same structural model with the functional BP86 with 10% Hartree-Fock exchange (hereafter called B10HFP86). The lower amount of Hartree-Fock (10% relative to 20% in B3LYP) increases the covalency of the metal-ligand bonds, resulting in a cluster with somewhat stronger backbonding to  $\text{N}_2\text{O}$  from  $\text{Cu}_I$  and  $\text{Cu}_{IV}$ , enhancing the stability of the bent  $\mu_{-1,3}$  isomer and producing stable reactant structures for both the terminal  $\text{Cu}_I$ -N and  $\mu_{-1,3}$   $\text{N}_2\text{O}$  isomers (Figure S9). The terminal  $\text{Cu}_I$ -N isomer is lower in electronic energy by 1.7 kcal/mol and lower in free energy by 6.8 kcal/mol, and again rearranges to the  $\mu_{-1,3}$  during N-O bond elongation.

In the  $\mu_{-1,3}$  isomer, which is the reactant for N-O bond cleavage (Figure 9A), backbonding is evident from  $\text{Cu}_I$  and  $\text{Cu}_{IV}$  into the  $\text{N}_2\text{O}$   $\pi^*$  orbital that is in the  $\text{Cu}_I/\text{Cu}_{IV}/\text{S}/\text{Cu}_{II}$  plane (ip), at a lower energy due to the bent N-N-O angle of 135° (Figure 9B, Table S4). This lowers the energy of the  $\text{N}_2\text{O}$   $\pi^*$  orbital that will receive the two electrons involved in N-O bond cleavage. Upon N-O bond elongation (B10HFP86), a transition state (TS) for N-O bond cleavage is obtained at an N-O bond length of 1.81 Å (Figure 9C, 1.68 Å for B3LYP). This TS occurs at a  $\Delta G^\ddagger$  of 17.7 kcal/mol and a  $\Delta E^\ddagger$  of 6.1 kcal/mol (relative to fully reduced and free  $\text{N}_2\text{O}$ ; 17.3 kcal/mol and 10.3 kcal/mol, respectively, for B3LYP). These values are in the range of the experimental values of  $\Delta G^\ddagger = 13 \pm 2$  kcal/mol and  $\Delta H^\ddagger = 10 \pm 1$  kcal/mol determined for the rate determining step of  $\text{N}_2\text{O}$  reduction. The TS is a broken symmetry singlet, where the  $\alpha$  LUMO, which for the reactant is dominantly ip

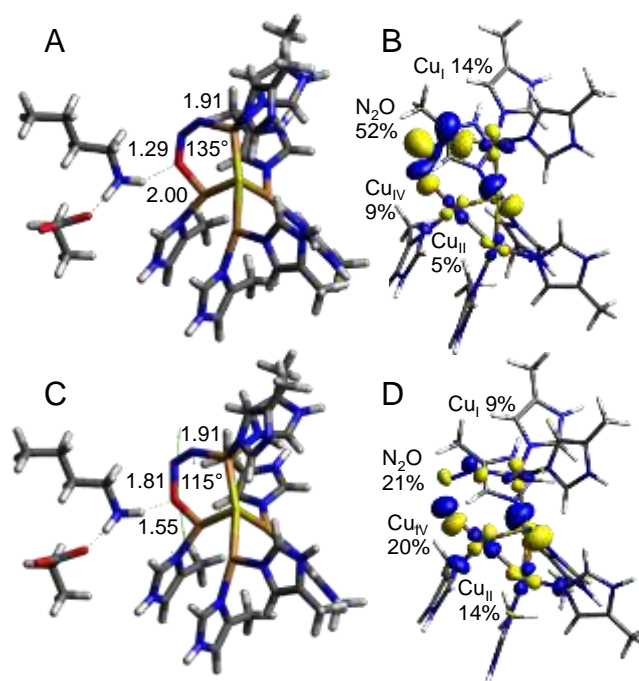


Figure 9: Structures for fully reduced cluster with  $\mu_{-1,3}$   $\text{N}_2\text{O}$  (A) and  $\mu_{-1,3}$  TS for N-O bond cleavage (C), giving N-O, O-H, and  $\text{Cu}_I$ -N bond lengths in Å and the N-N-O angle. Contours for the LUMO of the fully reduced cluster with  $\mu_{-1,3}$   $\text{N}_2\text{O}$  (B) and  $\alpha$  LUMO of the  $\mu_{-1,3}$  TS (D), with percentage on  $\text{N}_2\text{O}$ ,  $\text{Cu}_I$ ,  $\text{Cu}_{II}$ , and  $\text{Cu}_{IV}$ . BP86 with 10% Hartree-Fock exchange and PCM of 10.

$\text{N}_2\text{O}$   $\pi^*$  in character (52%  $\text{N}_2\text{O}$ , with 30% Cu from backbonding, Figure 9B and Table S4), is now dominantly Cu and S based (48% Cu character, mostly delocalized over  $\text{Cu}_{IV}$ , 20%, and  $\text{Cu}_{II}$ , 16%, via the  $\mu_4\text{S}^{2-}$ , Figure 9D and Table S4), indicating that an  $\alpha$  electron has been transferred from the fully reduced cluster to  $\text{N}_2\text{O}$  at the TS. This is supported by an increase in the Mulliken charge on  $\text{N}_2\text{O}$  from -0.28 in the bound reactant to -0.5 at the transition state (Table S5). The electron has been donated via  $\text{Cu}_{IV}$ , which has the best overlap with the  $\text{N}_2\text{O}$  ip  $\pi^*$  orbital at the TS, as elongation of the N-O bond in bent  $\text{N}_2\text{O}$  causes polarization of the ip  $\pi^*$  orbital towards O with respect to the reactants (the dominantly O based  $\text{N}_2\text{O}$   $\sigma^*$  orbital has come down in energy and mixes with the ip  $\pi^*$  orbital). Upon further N-O bond elongation past the TS, the  $\alpha$  hole becomes delocalized over all four coppers in the cluster and the  $\mu_4\text{S}^{2-}$  (Table S4), lowering the energy of the first electron transfer. At the TS, the  $\beta$  LUMO remains dominantly  $\text{N}_2\text{O}$  ip  $\pi^*$  in character (Table S4), indicating that, as in previous studies, only one electron is required to transfer at the TS to break the N-O bond. At the TS, the distance between the N of Lys397 and the O of  $\text{N}_2\text{O}$  has decreased from 2.92 Å to 2.63 Å, indicating that the strength of the Lys397-O hydrogen bond has increased, stabilizing the TS. However, the Lys N-H bond length is still short (1.10 Å at the TS relative to 1.03 Å for the reactants), indicating that the transition state is early on the proton transfer coordinate, consistent with the small positive SKIE observed experimentally.

After the TS, the reaction coordinate involves three discrete bond cleavage and formation processes: N-O cleavage, proton transfer from Lys397 to form an OH ligand at Cu<sub>IV</sub>, and cleavage of the Cu<sub>I</sub>-N bond to release N<sub>2</sub>. To investigate each of these coordinates, we performed 3D potential energy surface scans starting from the TS and scanning the N-O, O-H, and Cu<sub>I</sub>-N distances in 0.1 Å steps (Figure S10, where the different surfaces correspond to different Cu<sub>I</sub>-N distances). These surfaces show that further elongation of the N-O bond past the TS (at 1.81 Å) to 2.1 Å is required before proton transfer from Lys397 becomes downhill. The proton transfer is coupled with transfer of a β electron from Cu<sub>IV</sub> to N<sub>2</sub>O, which can be observed in changes in the β LUMO, which reflects uncompensated occupied orbital changes (Figure 10 at right, from top to bottom). At the start of the proton transfer (at N-O 2.1 Å, O-H 1.6 Å, and Cu<sub>I</sub>-N 2.0 Å), the α LUMO is delocalized over Cu<sub>IV</sub> (20%) and Cu<sub>II</sub> (19%) while the β LUMO is mainly oxyl in character (48% O, Figure 10A, Table S4, rows 4-5). As the proton transfers from Lys397 and N<sub>2</sub> is released, the β LUMO shifts from the oxyl to Cu<sub>IV</sub> to form a highly covalent Cu<sub>IV</sub>(II)-OH (24% O and 27% Cu<sub>IV</sub>, Figure 10B, Table S4, rows 6-7) and the total Mulliken spin density reflects a broken symmetry singlet with one hole (α) delocalized over Cu<sub>I</sub> and Cu<sub>III</sub> and the other (β) over Cu<sub>IV</sub> and Cu<sub>II</sub> (Table S5, row 3). Thus, the proton transfer drives the second electron transfer required to complete N<sub>2</sub>O reduction.

After proton transfer occurs at an N-O distance of 2.1 Å to form a hydroxide at Cu<sub>IV</sub>, cleavage of the Cu<sub>I</sub>-N bond is still required. A wider 2D potential energy scan of the N-O and Cu<sub>I</sub>-N bond lengths (over two different surfaces, one before and one after the proton transfer, Figure 11) shows that after further N-O elongation to 2.6 Å, loss of N<sub>2</sub> become energetically feasible (costing <2 kcal/mol). However, at this point N<sub>2</sub>

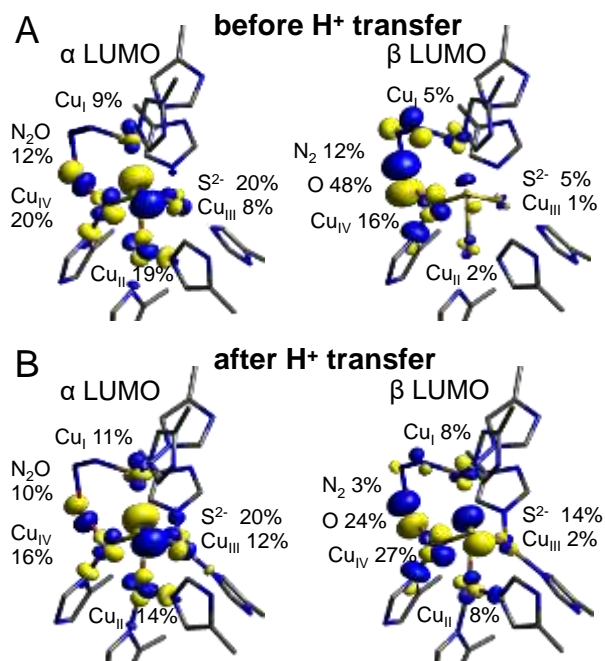


Figure 10: α and β LUMOs before (A) and after (B) proton transfer from Lys397, N-O 2.1 Å, Cu<sub>I</sub>-N 2.0 Å.

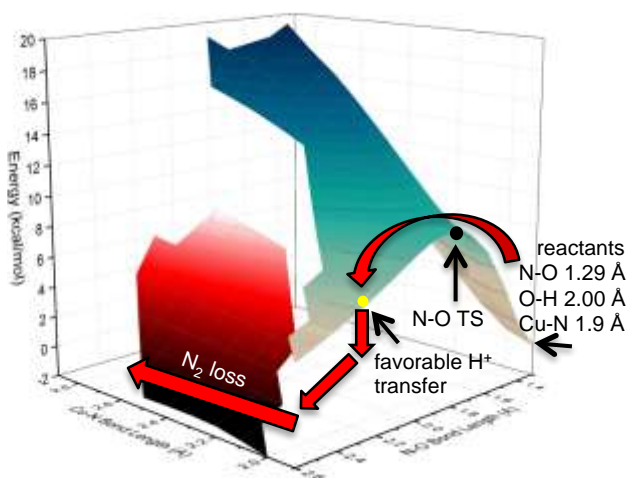


Figure 11: 2D potential energy surfaces for N-O bond cleavage and N<sub>2</sub> loss (Cu<sub>I</sub>-N elongation) before (blue) and after (red) proton transfer from Lys397 to Cu<sub>IV</sub>-OH. Red arrows track the lowest energy path from reactants to products, and key points are labeled in black. BP86 and 10% Hartree-Fock exchange, PCM = 10.

loss from Cu<sub>I</sub> is coupled to movement of the hydroxide ligand from terminal coordination at Cu<sub>IV</sub> to bridging Cu<sub>IV</sub> and Cu<sub>I</sub>, generating the undesired 2-hole μ<sub>2</sub>OH precursor to resting 1-hole Cu<sub>2</sub>\*. However, these calculations neglect the possibility of a rapid proton transfer from solvent and electron transfer from Cu<sub>A</sub>, both of which should take place after the proton transfer from Lys397 to form the Cu<sub>IV</sub>-OH product. When an extra proton or electron is added to the model after proton transfer from Lys397, intermediates are formed with a hydroxide ligand terminally coordinated to Cu<sub>IV</sub> and hydrogen bonded to Lys397 in either the 2-hole or 1-hole redox state (respectively, Figure 12). Further reduction or protonation, respectively, yields the 1-hole Cu<sub>IV</sub>-OH structure identified above as Cu<sub>2</sub><sup>0</sup> from spectroscopy, with loss of N<sub>2</sub>. The total proton and electron transfer process to form the 1-hole Cu<sub>IV</sub>-OH with a protonated Lys is highly favorable, with ΔG = -51 kcal/mol and ΔE = -50 kcal/mol (Figure 12).

Thus, a terminally coordinated hydroxide is obtained as the product of μ-1,3 N-O bond cleavage, as long as proton uptake from solvent is facile. This emphasizes the importance of the hydrogen bond from Lys397 to the Cu<sub>IV</sub>-OH and the Lys397-Glu435 salt bridge, which anchors the position of Lys397. The hydrogen bond stabilizes the higher energy Cu<sub>IV</sub>-OH product of N-O cleavage, which is required for rapid reduction of the catalytic site in turnover.

An alternative possibility to μ-1,3 binding and cleavage of N-O, proposed previously in two studies, is the coordination and cleavage of N<sub>2</sub>O via a μ-1,1-O or terminal Cu<sub>I</sub>-O isomer.<sup>34,42</sup> While our computational model does not yield a stable point for end-on N<sub>2</sub>O coordination via O to the fully reduced cluster in either a terminal or μ-1,1 mode, N<sub>2</sub>O can be positioned near the Cu<sub>I</sub>-Cu<sub>IV</sub> edge with O oriented towards

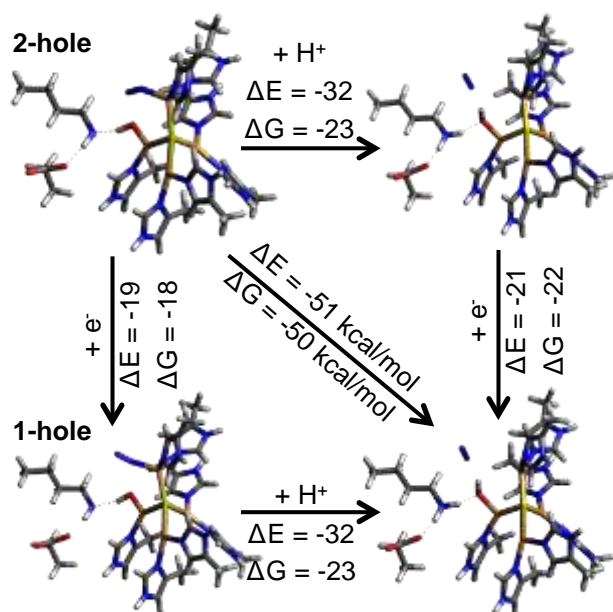
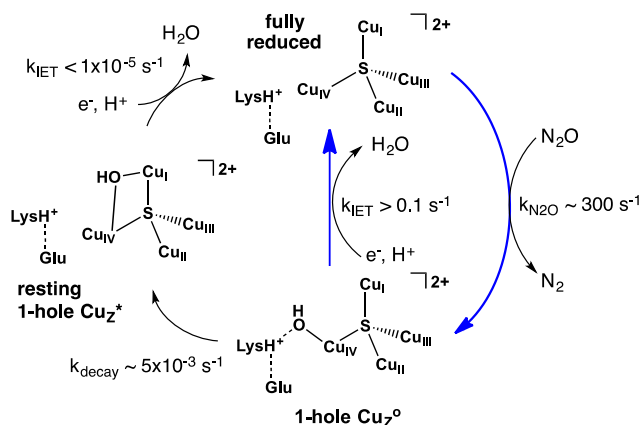


Figure 12: Scheme and energies for sequential protonation and reduction of the transient species with N-O 2.1 Å, O-H 1.02 Å, and Cu<sub>I</sub>-N 2.0 Å formed after proton transfer from Lys397.

Cu<sub>I</sub> and upon N-O elongation a TS is found for terminal N-O bond cleavage which has an N-O bond length of 1.34 Å, a Cu<sub>I</sub>-O bond length of 2.07 and a Cu<sub>IV</sub>-O distance of 2.42 Å (Figure S11). The terminal TS is ~9 kcal/mol higher in energy than the μ-1,3 TS described above, with a ΔG<sup>‡</sup> of 26.4 kcal/mol and a ΔE<sup>‡</sup> of 19.7 kcal/mol using the B3LYP functional. The higher energy of the terminal TS arises from the absence of a hydrogen bond to the O of N<sub>2</sub>O, as Lys397 is 4.25 Å away. A prior computational study found the μ-1,3 and terminal TS to be at similar energies, utilizing H<sub>2</sub>O to hydrogen bond to the O in both transition states.<sup>34</sup> However, Lys397 is constrained by the protein and is only available as a hydrogen bond donor to N<sub>2</sub>O in the μ-1,3 binding mode (to the O coordinated to Cu<sub>IV</sub>). Additionally, a terminal Cu<sub>I</sub>-O or μ-1,1-O-bridged structure would give a bridging oxo or hydroxo product after N-O cleavage, which would result in resting 1-hole Cu<sub>Z</sub>\* rather than 1-hole Cu<sub>Z</sub><sup>°</sup>, where only the latter is capable of turnover.

#### 4. Discussion.

In this study, we have shown that the transient 1-hole Cu<sub>Z</sub><sup>°</sup> intermediate that initially forms ( $k_{\text{obs}} \sim 200 \text{ s}^{-1}$ )<sup>23</sup> upon N<sub>2</sub>O reduction by fully reduced Cu<sub>4</sub>S-containing *Mh*N<sub>2</sub>OR can be rapidly reduced by the physiologically relevant electron donor sodium ascorbate, likely by intramolecular electron transfer from Cu<sub>A</sub>. This reduction is faster than the decay of Cu<sub>Z</sub><sup>°</sup> to the inactive resting 1-hole Cu<sub>Z</sub>\* state of the Cu<sub>4</sub>S cluster (Scheme 1). This indicates that N<sub>2</sub>O reduction by the Cu<sub>4</sub>S active site of N<sub>2</sub>OR bypasses the resting 1-hole Cu<sub>Z</sub>\* state, which is not reduced by physiologically relevant reductants; instead, the 1-hole Cu<sub>Z</sub><sup>°</sup> intermediate is the relevant 1-hole oxidized state of the Cu<sub>4</sub>S cluster during turnover. Here, we have defined the nature of this 1-hole Cu<sub>Z</sub><sup>°</sup> intermediate and



Scheme 1: Pathways of Cu<sub>Z</sub><sup>°</sup> formation, reduction, and decay to resting 1-hole Cu<sub>Z</sub>\* with relevant rates, with blue arrows showing steps involved in catalytic turnover.

elucidated how it differs from the resting 1-hole Cu<sub>Z</sub>\* state and thus determined the origin of its rapid reduction via Cu<sub>A</sub>. Further, the nature of Cu<sub>Z</sub><sup>°</sup> produces an important insight into the mechanism of N<sub>2</sub>O reduction by the Cu<sub>4</sub>S active site of N<sub>2</sub>OR and the role of the tetranuclear μ<sub>4</sub>S<sup>2-</sup> bridged cluster in this process.

**4.1 Identification of 1-hole Cu<sub>Z</sub><sup>°</sup> and differences with resting 1-hole Cu<sub>Z</sub>\*.** EPR, absorption, MCD and resonance Raman spectroscopies correlated to DFT calculations have been used to develop a model for the 1-hole Cu<sub>Z</sub><sup>°</sup> intermediate. The EPR A<sub>||</sub> values for Cu<sub>Z</sub><sup>°</sup> show that the spin is delocalized over two coppers, differing from the ~5:2 distribution of spin over Cu<sub>I</sub> and Cu<sub>IV</sub> observed in resting 1-hole Cu<sub>Z</sub>\*.<sup>35</sup> Differences in the relative intensities of the μ<sub>4</sub>S<sup>2-</sup> to Cu CT transitions between Cu<sub>Z</sub><sup>°</sup> and resting 1-hole Cu<sub>Z</sub>\* indicate (from the pseudo-A term MCD analysis) that this spin redistribution is due to a decrease in spin density on Cu<sub>I</sub> and an increase in spin density on Cu<sub>IV</sub>. The resonance Raman spectrum of the Cu<sub>Z</sub><sup>°</sup> intermediate shows two Cu-S stretching vibrations, an intense mode at 426 cm<sup>-1</sup> and a weak mode at 413 cm<sup>-1</sup> which exhibits a -3 cm<sup>-1</sup> shift when Cu<sub>Z</sub><sup>°</sup> is formed in O<sup>18</sup> labeled water. H<sub>2</sub>O<sup>18</sup> isotope sensitivity in a Cu-S stretching mode indicates that there is a solvent-exchangeable hydroxide ligand on the Cu<sub>I</sub>-Cu<sub>IV</sub> edge, as this leads to Cu-O stretches that are high enough in energy to mix with the Cu-S vibrations of the Cu<sub>4</sub>S core. Chemically reasonable models for the Cu<sub>Z</sub><sup>°</sup> intermediate were investigated with DFT calculations, and, from correlation to the spectral features of Cu<sub>Z</sub><sup>°</sup>, only a Cu<sub>IV</sub>-OH model stabilized by hydrogen bonding to a protonated second sphere Lys397 reproduces the shift of the spin density from Cu<sub>I</sub> to Cu<sub>IV</sub> and the H<sub>2</sub>O<sup>18</sup> isotope shift in a high energy Cu-S vibration. We thus identify the 1-hole Cu<sub>Z</sub><sup>°</sup> intermediate as having a hydroxide ligand bound terminally to Cu<sub>IV</sub> and hydrogen bonded to Lys397 (Figure 8C and Scheme 1).

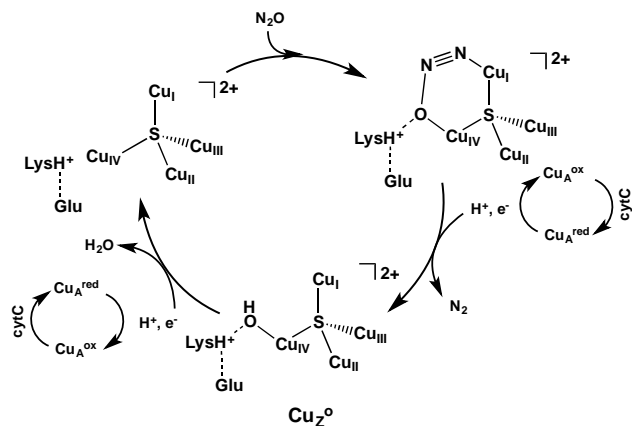
This model elucidates the nature of the differences between 1-hole Cu<sub>Z</sub><sup>°</sup> (the transient intermediate formed from N<sub>2</sub>O reduction) and 1-hole Cu<sub>Z</sub>\* (the stable resting form that results from Cu<sub>Z</sub><sup>°</sup> decay). Both of these 1-hole states of the

$\text{Cu}_4\text{S}$  cluster have a hydroxide edge ligand, but in  $\text{Cu}_2^\circ$  the hydroxide is terminally coordinated to  $\text{Cu}_{\text{IV}}$  (calculated  $\text{Cu}_{\text{IV}}\text{-OH}$  of 1.93 Å) while in resting 1-hole  $\text{Cu}_2^*$  the hydroxide asymmetrically bridges the  $\text{Cu}_\text{I}\text{-Cu}_{\text{IV}}$  edge, with a stronger interaction with  $\text{Cu}_\text{I}$  than with  $\text{Cu}_{\text{IV}}$  ( $\text{Cu}_\text{I}\text{-OH}$  of 2.00 Å,  $\text{Cu}_{\text{IV}}\text{-OH}$  of 2.09 Å). The barrier for decay of 1-hole  $\text{Cu}_2^\circ$  to the  $\mu_2\text{OH}$  bridged resting 1-hole  $\text{Cu}_2^*$  (Scheme 1, bottom) thus arises from breaking the hydrogen bond to Lys397 before the bond with  $\text{Cu}_\text{I}$  is formed. This is consistent with the pH dependence observed for steady-state turnover, which indicates that Lys397 must be protonated for catalytic activity. It also provides an explanation for the reported pH dependence of the turnover-dependent inactivation of  $Mh\text{N}_2\text{OR}$ , which suggests that the decay of the  $\text{Cu}_2^\circ$  intermediate is more rapid at higher pH,<sup>27</sup> as deprotonation of Lys397 will lower the barrier for decay of  $\text{Cu}_2^\circ$  to resting 1-hole  $\text{Cu}_2^*$ .

The key difference in reactivity between the 1-hole  $\text{Cu}_2^\circ$  intermediate and resting 1-hole  $\text{Cu}_2^*$  is that  $\text{Cu}_2^\circ$  is rapidly reduced in turnover while resting 1-hole  $\text{Cu}_2^*$  is not. Reduction studies with sodium ascorbate as the electron donor show that 1-hole  $\text{Cu}_2^\circ$  is rapidly reduced, likely via intramolecular electron transfer from  $\text{Cu}_\text{A}$  (with a lower limit on the  $k_{\text{ET}}$  of  $0.1\text{ s}^{-1}$ ; to be consistent with the steady-state activity of  $Mh\text{N}_2\text{OR}$ , this intramolecular ET rate must be greater than  $k_{\text{cat}} = 320\text{ s}^{-1}$ ),<sup>26</sup> while resting 1-hole  $\text{Cu}_2^*$  is not reduced by electron transfer from  $\text{Cu}_\text{A}$  (with an upper limit on  $k_{\text{ET}}$  of  $1 \times 10^{-5}\text{ s}^{-1}$ ). The greater than  $10^4$ -fold faster rate of reduction of  $\text{Cu}_2^\circ$  compared to resting 1-hole  $\text{Cu}_2^*$  reflects the higher energy (calculated at +6.4 kcal/mol) of the metastable  $\text{Cu}_2^\circ$  intermediate, which provides a greater driving force for electron transfer from  $\text{Cu}_\text{A}$  to  $\text{Cu}_2^\circ$  relative to resting 1-hole  $\text{Cu}_2^*$ . Thus, in turnover the second sphere of the  $\text{Cu}_4\text{S}$  cluster is tuned to stabilize the higher energy  $\text{Cu}_2^\circ$  intermediate, a kinetic product of turnover, so that it has a long enough lifetime that reduction by  $\text{Cu}_\text{A}$  can occur faster than the decay of  $\text{Cu}_2^\circ$  to inactive resting 1-hole  $\text{Cu}_2^*$ . Importantly, second-sphere stabilization of  $\text{Cu}_2^\circ$  reflects the effect of the Lys397 hydrogen bond to the terminal hydroxide coordinated at  $\text{Cu}_{\text{IV}}$ .

**4.2 Mechanistic insight into  $\text{N}_2\text{O}$  reduction.** The identification of 1-hole  $\text{Cu}_2^\circ$  as a  $\text{Cu}_{\text{IV}}\text{-OH}$  intermediate formed from N-O bond cleavage which can be rapidly reduced by  $\text{Cu}_\text{A}$  produces further insight into the mechanism of  $\text{N}_2\text{O}$  reduction by the  $\text{Cu}_4\text{S}$  cluster in  $\text{N}_2\text{OR}$ . First, it emphasizes the importance of a key asymmetry in the  $\text{N}_2\text{OR}$  active site. The second sphere residue Lys397 is positioned to provide a hydrogen bond only to a ligand coordinated to the  $\text{Cu}_{\text{IV}}$  of the open  $\text{Cu}_\text{I}\text{-Cu}_{\text{IV}}$  edge. This stabilizes the  $\text{Cu}_2^\circ$  intermediate by creating a barrier to the decay of its terminal  $\text{Cu}_{\text{IV}}\text{-OH}$  to form the  $\mu_2\text{OH}$  bridged resting state. The presence of protonated Lys397 near  $\text{Cu}_{\text{IV}}$  also influences the mechanism of  $\text{N}_2\text{O}$  reduction at the  $\text{Cu}_\text{I}\text{-Cu}_{\text{IV}}$  edge to lead to a non-bridging product. Previous computational descriptions of the reaction coordinate for N-O bond cleavage by the  $4\text{Cu}^\text{I}$  state of the  $\text{Cu}_4\text{S}$  cluster included either no hydrogen bond donation or hydrogen bond donation by a flexible donor molecule (water or formate).<sup>8,34</sup> These studies proposed several possible

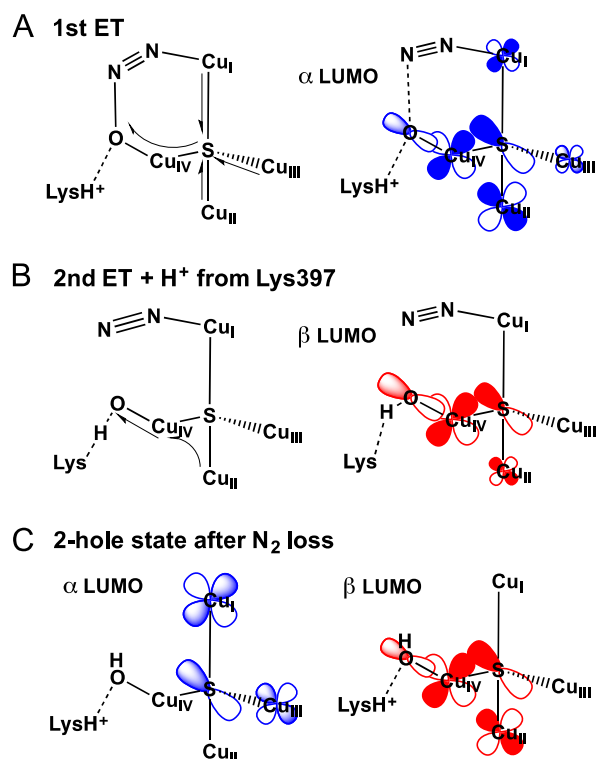
modes for  $\text{N}_2\text{O}$  coordination at the  $\text{Cu}_\text{I}\text{-Cu}_{\text{IV}}$  edge, including terminal  $\text{O-Cu}_\text{I}$ ,  $\mu\text{-}1,1\text{-O}$  bridging  $\text{Cu}_\text{I}$  and  $\text{Cu}_{\text{IV}}$ , and  $\mu\text{-}1,3$  bridging ( $\text{Cu}_{\text{IV}}\text{-O}$  and  $\text{Cu}_\text{I}\text{-N}$ ). However, in these reaction coordinate calculations, the product of N-O bond cleavage was either a bridging oxo or hydroxo 2-hole intermediate. Upon subsequent protonation and reduction by  $\text{Cu}_\text{A}$ , these would produce the inactive resting 1-hole  $\text{Cu}_2^*$  state. In the present study, the reaction coordinate developed in Section 3.3.3 includes the presence of protonated Lys397 and starts with  $\mu\text{-}1,3$  coordination of  $\text{N}_2\text{O}$  to the fully reduced ( $\text{Cu}_\text{I}^\text{I}$ ) cluster. In this binding mode, the  $\text{Cu}_{\text{IV}}\text{-O}$  interaction and the Lys397 hydrogen bond is already formed before N-O bond cleavage, precluding the interaction between the O of  $\text{N}_2\text{O}$  and  $\text{Cu}_\text{I}$ . Upon N-O bond cleavage, proton transfer from Lys397, and proton coupled electron transfer from  $\text{Cu}_\text{A}$ , the 1-hole  $\text{Cu}_2^\circ$  intermediate is formed with a terminal hydroxide coordinated to  $\text{Cu}_{\text{IV}}$ . The transition state obtained for this N-O bond cleavage process is consistent with the experimental temperature dependence of the reduction of  $\text{N}_2\text{O}$  by  $\text{N}_2\text{OR}$  under steady-state turnover conditions, which gives the kinetic parameters  $\Delta E_\text{A} = 10 \pm 2$  kcal/mol and  $\Delta G^\ddagger = 13 \pm 2$  kcal/mol and a small normal solvent kinetic isotope effect of 1.1 for the rate limiting step. This mechanism is summarized in Scheme 2.



**Scheme 2: Mechanism of  $\text{N}_2\text{O}$  reduction by the  $\text{Cu}_4\text{S}$  active site of  $\text{N}_2\text{OR}$ .**

**4.3 Role of the  $\text{Cu}_4\text{S}$  cluster in  $\text{N}_2\text{O}$  reduction.** The formation of a terminal  $\text{Cu}_{\text{IV}}\text{-OH}$  intermediate after N-O bond cleavage indicates that the two electron transfer from the  $4\text{Cu}^\text{I}$  cluster required for  $\text{N}_2\text{O}$  reduction proceeds by a significantly different mechanism than previously proposed. Computational studies of N-O bond cleavage with  $\text{N}_2\text{O}$  coordinated between  $\text{Cu}_\text{I}$  and  $\text{Cu}_{\text{IV}}$  indicated that one electron is transferred from  $\text{Cu}_{\text{IV}}$  at the transition state and the other transfers from  $\text{Cu}_\text{I}$  upon formation of the  $\text{Cu}_\text{I}\text{-O}^{2-}$  bond later in the reaction coordinate.<sup>8,34</sup> However, the experimentally observed  $\text{Cu}_2^\circ$  intermediate has a terminal hydroxide bound to  $\text{Cu}_{\text{IV}}$  and lacks a  $\text{Cu}_\text{I}\text{-O}^{2-}$  interaction, so in N-O bond cleavage both electrons must be transferred to  $\text{N}_2\text{O}$  via  $\text{Cu}_{\text{IV}}$ .

Examination of the electronic structure changes during N-O bond cleavage (Figure 9 and 10) indicates that this two electron transfer process involves all four coppers in the cluster. The first electron is transferred via  $\text{Cu}_{\text{IV}}$  to break the N-O



**Scheme 3: MO depictions of the first and second electron transfer from the fully reduced ( $4\text{Cu}^{\text{I}}$ )  $\text{Cu}_4\text{S}$  cluster to  $\mu\text{-}1,3$   $\text{N}_2\text{O}$ . A) The first electron transfer via  $\text{Cu}_{\text{IV}}$ , B) The second electron transfer via  $\text{Cu}_{\text{IV}}$  with concerted protonation of Lys397, and C) the  $\alpha$  and  $\beta$  LUMOs of the product 2-hole  $\text{Cu}_{\text{IV}}\text{-OH}$  state.**

bond at the transition state. The involvement of  $\text{Cu}_{\text{IV}}$  is due to the increased O character in the  $\text{N}_2\text{O}$  LUMO upon N-O bond elongation. The resulting first electron is delocalized over the other three coppers in the  $\text{Cu}_4\text{S}$  cluster via the  $\mu_4\text{S}^{2-}$  bridge, which provides a good superexchange pathway, lowering the energy of the first electron transfer (Scheme 3A). Subsequently, proton transfer from Lys397 to form the terminal hydroxide ligand at  $\text{Cu}_{\text{IV}}$  results in the transfer of a second electron, again via  $\text{Cu}_{\text{IV}}$ , which occurs after the N-O bond is broken (Scheme 3B). Proton uptake from solvent and loss of  $\text{N}_2$  leads to a 2-hole intermediate where one hole is delocalized over  $\text{Cu}_{\text{I}}$  and  $\text{Cu}_{\text{III}}$  and the other is delocalized over  $\text{Cu}_{\text{I}}$  and  $\text{Cu}_{\text{IV}}$  (Scheme 3C).

This mechanism for two electron transfer via a single Cu center elucidates the role of a tetranuclear copper cluster as the active site for  $\text{N}_2\text{OR}$ . In other systems, e.g. the zeolite  $\text{Cu-ZSM-5}$ ,  $\text{N}_2\text{O}$  is reduced by a binuclear copper site with no bridging ligands to provide a superexchange pathway between the copper centers.<sup>43</sup> In the zeolite system,  $\text{N}_2\text{O}$  must coordinate in a  $\mu\text{-}1,1\text{-O}$  mode, so that one electron can transfer from one Cu at the TS and the second electron from the other, leading to an oxo bridged product that is active in the zeolite but would be inactive in the  $\text{N}_2\text{OR}$  enzymatic system. To avoid this, the  $\text{Cu}_4\text{S}$  cluster stabilizes the O at  $\text{Cu}_{\text{IV}}$  using second sphere hydrogen bonding and thus has a very covalent  $\mu_4$ -bridging sulfide ligand, which provides sufficiently

good superexchange that both electrons can be transferred to  $\text{N}_2\text{O}$  via one copper center ( $\text{Cu}_{\text{IV}}$ ). While this could potentially be accomplished by a binuclear copper site with a bridging sulfide, our previous computational study of the  $\text{Cu}_4\text{S}$  cluster suggests that the sulfide in a  $\text{Cu}_2\text{S}$  cluster would be highly susceptible to protonation and the resulting  $\mu_2\text{SH}$  would not be an effective superexchange pathway.<sup>8</sup> The presence of two additional coppers in the tetranuclear cluster protects the  $\mu_4\text{S}^{2-}$  from protonation, maintaining the good superexchange that is necessary for two electron transfer via a single copper center.

Thus, the  $\text{Cu}_4\text{S}$  active site of  $\text{N}_2\text{OR}$  is optimized to reduce  $\text{N}_2\text{O}$  asymmetrically, generating a 1-hole intermediate,  $\text{Cu}_2^\circ$ , that has a hydroxide ligand terminally coordinated to  $\text{Cu}_{\text{IV}}$ .  $\text{Cu}_2^\circ$  can be rapidly reduced in turnover via electron transfer from  $\text{Cu}_{\text{A}}$ , providing a mechanism by which the  $\text{Cu}_4\text{S}$  cluster can reduce  $\text{N}_2\text{O}$  using physiologically relevant electron donors. This excludes the inactive resting 1-hole  $\text{Cu}_2^*$  state from the catalytic cycle and shows that the  $\text{Cu}_4\text{S}$  form of the  $\text{N}_2\text{OR}$  active site is competent for nitrous oxide reduction *in vivo*.

**5. Conclusions.** EPR, absorption, MCD and resonance Raman spectroscopies coupled to DFT calculations have defined the nature of the  $\text{Cu}_2^\circ$  intermediate observed in the single turnover reaction of fully reduced  $\text{N}_2\text{OR}$  with  $\text{N}_2\text{O}$ . The  $\text{Cu}_2^\circ$  intermediate has a hydroxide ligand terminally coordinated to  $\text{Cu}_{\text{IV}}$ , stabilized by a second sphere hydrogen bond to the protonated Lys397. The decay of this intermediate, which leads to inactivation of  $\text{N}_2\text{OR}$ , involves breaking the hydrogen bond between Lys397 and the hydroxide to form the  $\mu_2\text{OH}$  bridged resting 1-hole  $\text{Cu}_2^*$  state. Unlike resting 1-hole  $\text{Cu}_2^*$ , the 1-hole  $\text{Cu}_2^\circ$  intermediate can be rapidly reduced, via electron transfer from  $\text{Cu}_{\text{A}}$ , by physiologically relevant reductants. The higher energy of metastable  $\text{Cu}_2^\circ$  relative to resting 1-hole  $\text{Cu}_2^*$  provides the additional driving force necessary for the rapid reduction of  $\text{Cu}_2^\circ$  in turnover. The terminal hydroxide coordination in  $\text{Cu}_2^\circ$  suggests a mechanism for  $\text{N}_2\text{O}$  reduction by the fully reduced  $\text{Cu}_4\text{S}$  cluster, in which  $\text{N}_2\text{O}$  bridges in a  $\mu\text{-}1,3$   $\text{Cu}_{\text{IV}}\text{-ON}_2\text{-Cu}_{\text{I}}$  structure and the two electrons required for N-O bond cleavage are both transferred through the  $\mu_4\text{S}^{2-}$  bridge via the  $\text{Cu}_{\text{IV}}$  center.

## ASSOCIATED CONTENT

**Supporting Information.**  $\text{Cu}_2^\circ$  spectra with details of  $\text{Cu}_{\text{A}}$  subtraction; table of bands and assignments for  $\text{Cu}_2^\circ$  and  $\text{Cu}_2^*$  absorption and MCD spectra; resonance Raman spectrum and profile for resting 1-hole  $\text{Cu}_2^*$ ; kinetic schemes and supplemental experiments for  $\text{Cu}_2^\circ$  reduction by ascorbate; description of computational modeling of resting 1-hole  $\text{Cu}_2^*$ ; details of DFT calculations including  $\text{Cu}_4\text{S}$  models for  $\text{Cu}_2^\circ$  and their vibrational assignments; calculated transition state for  $\text{Cu}_2^\circ$  decay; estimates of  $\lambda_{\text{total}}$ ,  $H_{\text{DA}}$ , and  $\Delta\Delta G^\circ$  for Marcus Theory analysis; 3D PES and tables of Mulliken atomic spin density and Mulliken charges during 2 electron transfer from  $\text{Cu}_4\text{S}$  to  $\text{N}_2\text{O}$ ;  $\mu\text{-}1,1\text{-O}$  TS for N-O cleavage; coordinates for key structures used for DFT calculations. This material is available free of charge via the Internet at <http://pubs.acs.org>.

## AUTHOR INFORMATION

### Corresponding Author

\* edward.solomon@stanford.edu

### Present Addresses

† Department of Chemistry, University of York, York, UK.

\* Dipartimento di Chimica, Università di Pavia, Via Taramelli 12, 27100 Pavia, Italy.

& Indian Association for the Cultivation of Science, Kolkata, India.

### Author Contributions

E.M.J. performed EPR, absorption, MCD, and resonance Raman experiments, analyzed spectroscopic data, performed DFT calculations, and conceived the ascorbate reduction of Cu<sup>2+</sup> experiments in collaboration with E.I.S. S.D. and C.C. purified Mn<sub>2</sub>O<sub>3</sub> and C.C. performed absorption time dependence experiments. S.G.D. performed steady-state turnover experiments. S.R.P., I.M. and E.I.S. designed experiments and oversaw the work. E.M.J. and E.I.S. wrote the manuscript with contributions from all authors.

### ACKNOWLEDGMENT

This research was supported by the NIH grant DK-31450 (E.I.S.), a Stanford Graduate Fellowship (E.M.J.), and financial support from the Fundação para a Ciência e Tecnologia to IM (PTDC/QUI-BIQ/116481/2010 and PTDC/BBB-BQB/0129/2014) and to CC (SFRH/BD/87898/2012). This work was also supported by the Unidade de Ciências Biomoleculares Aplicadas-UCIBIO, which is financed by national funds from FCT/MEC (UID/Multi/04378/2013) and co-financed by the ERDF under the PT2020 Partnership Agreement (POCI-01-0145-FEDER-007728). SRP is an IF fellow supported by FCT. The content is solely the responsibility of the authors and does not necessarily represent the official views of the National Institutes of Health. The authors declare no competing financial interest.

### REFERENCES

- (1) Bates, B.; Kundzewicz, Z. W.; Wu, S.; Arnell, N.; Burkett, V.; Döll, P.; Gwary, D.; Hanson, C.; Heij, B.; Jiménez, B.; Kaser, G.; Kitoh, A.; Kovats, S.; Kumar, P.; Magadza, C.; Martino, D.; Mata, L. J.; Medany, M.; Miller, K.; Oki, T.; Osman, B.; Palutikof, J.; Prowse, T.; Pulwarty, R.; Räisänen, J.; Renwick, J.; Tubiello, F.; Wood, R.; Zhao, Z.-C.; Arblaster, J.; Betts, R.; Dai, A.; Milly, C.; Mortsch, L.; Nurse, L.; Payne, R.; Pinskiwar, I.; Wilbanks, T.; Secretariat, I., Ed. 2008.
- (2) Ravishankara, A. R.; Daniel, J. S.; Portmann, R. *W. Science* **2009**, *326*, 123.
- (3) Richardson, D.; Felgate, H.; Watmough, N.; Thomson, A.; Baggs, E. *Trends in Biotechnology* **2009**, *27*, 388.
- (4) Thomson, A. J.; Giannopoulos, G.; Pretty, J.; Baggs, E. M.; Richardson, D. J. *Philosophical Transactions of the Royal Society B-Biological Sciences* **2012**, *367*, 1157.
- (5) Tavares, P.; Pereira, A. S.; Moura, J. J. G.; Moura, I. *Journal of Inorganic Biochemistry* **2006**, *100*, 2087.
- (6) Zumft, W. G.; Kroneck, P. M. H. *Advances in Microbial Physiology* **2007**, *52*, 107.
- (7) Pauleta, S. R.; Dell'Acqua, S.; Moura, I. *Coordination Chemistry Reviews* **2013**, *257*, 332.
- (8) Gorelsky, S. I.; Ghosh, S.; Solomon, E. I. *Journal of the American Chemical Society* **2006**, *128*, 278.
- (9) Prudencio, M.; Pereira, A. S.; Tavares, P.; Besson, S.; Cabrito, I.; Brown, K.; Samyn, B.; Devreese, B.; Van Beeumen, J.; Rusnak, F.; Fauque, G.; Moura, J. J. G.; Tegoni, M.; Cambillau, C.; Moura, I. *Biochemistry* **2000**, *39*, 3899.
- (10) Brown, K.; Tegoni, M.; Prudencio, M.; Pereira, A. S.; Besson, S.; Moura, J. J.; Moura, I.; Cambillau, C. *Nature Structural Biology* **2000**, *7*, 191.
- (11) Rasmussen, T.; Berks, B. C.; Sanders-Loehr, J.; Dooley, D. M.; Zumft, W. G.; Thomson, A. J. *Biochemistry* **2000**, *39*, 12753.
- (12) Brown, K.; Djinic-Carugo, K.; Haltia, T.; Cabrito, I.; Saraste, M.; Moura, J. J. G.; Moura, I.; Tegoni, M.; Cambillau, C. *Journal of Biological Chemistry* **2000**, *275*, 41133.
- (13) Alvarez, M. L.; Ai, J. Y.; Zumft, W.; Sanders-Loehr, J.; Dooley, D. M. *Journal of the American Chemical Society* **2001**, *123*, 576.
- (14) Farrar, J. A.; Neese, F.; Lappalainen, P.; Kroneck, P. M. H.; Saraste, M.; Zumft, W. G.; Thomson, A. J. *Journal of the American Chemical Society* **1996**, *118*, 11501.
- (15) Kroneck, P. M. H.; Kastrau, D. H. W.; Antholine, W. E. *Journal of Inorganic Biochemistry* **1992**, *47*, 19.
- (16) Psomas, G.; Kessissoglou, D. P. *Dalton Transactions* **2013**, *42*, 6252.
- (17) Chen, P.; Cabrito, I.; Moura, J. J. G.; Moura, I.; Solomon, E. I. *Journal of the American Chemical Society* **2002**, *124*, 10497.
- (18) Rasmussen, T.; Berks, B. C.; Butt, J. N.; Thomson, A. J. *Biochemical Journal* **2002**, *364*, 807.
- (19) Oganesyan, V. S.; Rasmussen, T.; Fairhurst, S.; Thomson, A. J. *Dalton Transactions* **2004**, 996.
- (20) Ghosh, S.; Gorelsky, S. I.; George, S. D.; Chan, J. M.; Cabrito, I.; Dooley, D. M.; Moura, J. J. G.; Moura, I.; Solomon, E. I. *Journal of the American Chemical Society* **2007**, *129*, 3955.
- (21) Pomowski, A.; Zumft, W. G.; Kroneck, P. M. H.; Einsle, O. *Nature* **2011**, *477*, 234.
- (22) Dell'Acqua, S.; Pauleta, S. R.; Moura, J. J. G.; Moura, I. *Philosophical Transactions of the Royal Society B-Biological Sciences* **2012**, *367*, 1204.
- (23) Johnston, E. M.; Dell'Acqua, S.; Ramos, S.; Pauleta, S. R.; Moura, I.; Solomon, E. I. *Journal of the American Chemical Society* **2014**, *136*, 614.
- (24) Chan, J. M.; Bollinger, J. A.; Grewell, C. L.; Dooley, D. M. *Journal of the American Chemical Society* **2004**, *126*, 3030.
- (25) Ghosh, S.; Gorelsky, S. I.; Chen, P.; Cabrito, I.; Moura, J. J. G.; Moura, I.; Solomon, E. I. *Journal of the American Chemical Society* **2003**, *125*, 15708.
- (26) Dell'Acqua, S.; Pauleta, S. R.; Monzani, E.; Pereira, A. S.; Casella, L.; Moura, J. J. G.; Moura, I. *Biochemistry* **2008**, *47*, 10852.
- (27) Dell'Acqua, S.; Pauleta, S. R.; Paes de Sousa, P. M.; Monzani, E.; Casella, L.; Moura, J. J. G.; Moura, I. *Journal of Biological Inorganic Chemistry* **2010**, *15*, 967.
- (28) Frisch, M. J.; Trucks, G. W.; Schlegel, H. B.; Scuseria, G. E.; Robb, M. A.; Cheeseman, J. R.; Scalmani, G.; Barone, V.; Mennucci, B.; Petersson, G. A.; Nakatsuji, H.; Caricato, M.; Li, X.; Hratchian, H. P.; Izmaylov, A. F.; Bloino, J.; Zheng, G.; Sonnenberg, J. L.; Hada, M.; Ehara, M.; Toyota, K.; Fukuda, R.; Hasegawa, J.; Ishida, M.; Nakajima, T.; Honda, Y.; Kitao, O.; Nakai, H.; Vreven, T.; Montgomery Jr., J. A.; Peralta, J. E.; Ogliaro, F.; Bearpark, M. J.; Heyd, J.; Brothers, E. N.; Kudin, K. N.; Staroverov, V. N.; Kobayashi, R.; Normand, J.; Raghavachari, K.; Rendell, A. P.; Burant, J. C.; Iyengar, S. S.; Tomasi, J.; Cossi, M.; Rega, N.; Millam, N. J.; Klene, M.; Knox, J. E.; Cross, J. B.; Bakken, V.; Adamo, C.; Jaramillo, J.;



- Gomperts, R.; Stratmann, R. E.; Yazyev, O.; Austin, A. J.; Cammi, R.; Pomelli, C.; Ochterski, J. W.; Martin, R. L.; Morokuma, K.; Zakrzewski, V. G.; Voth, G. A.; Salvador, P.; Dannenberg, J. J.; Dapprich, S.; Daniels, A. D.; Farkas, Ö.; Foresman, J. B.; Ortiz, J. V.; Cioslowski, J.; Fox, D. J.; Gaussian, Inc.: Wallingford, CT, USA, 2009.
- (29) Hanwell, M. D.; Curtis, D. E.; Lonie, D. C.; Vandermeersch, T.; Zurek, E.; Hutchison, G. R. *Journal of Cheminformatics* **2012**, *4*.
- (30) Li, Y.; Cirino, P. C. *Biotechnology and Bioengineering* **2014**, *111*, 1273.
- (31) Humphrey, W.; Dalke, A.; Schulten, K. "VMD - Visual Molecular Dynamics", 1996; Vol. 14.
- (32) Tenderholt, A. L. *QMForge: A Program to Analyze Quantum Chemistry Calculations*; Version 2.3.2 ed.
- (33) Park, K.; Solomon, E. I. *Canadian Journal of Chemistry* **2014**, *92*, 975.
- (34) Ertem, M. Z.; Cramer, C. J.; Himo, F.; Siegbahn, P. E. M. *Journal of Biological Inorganic Chemistry* **2012**, *17*, 687.
- (35) Chen, P.; George, S. D.; Cabrito, I.; Antholine, W. E.; Moura, J. J. G.; Moura, I.; Hedman, B.; Hodgson, K. O.; Solomon, E. I. *Journal of the American Chemical Society* **2002**, *124*, 744.
- (36) Johnston, E. M.; Dell'Acqua, S.; Pauleta, S. R.; Moura, I.; Solomon, E. I. *Chemical Science* **2015**, *6*, 5670.
- (37) Marcus, R. A.; Sutin, N. *Biochimica Et Biophysica Acta* **1985**, *811*, 265.
- (38) Auer, B.; Fernandez, L. E.; Hammes-Schiffer, S. *Journal of the American Chemical Society* **2011**, *133*, 8282.
- (39) Fernandez, L. E.; Horvath, S.; Hammes-Schiffer, S. *Journal of Physical Chemistry C* **2012**, *116*, 3171.
- (40) Heppner, D. E.; Kjaergaard, C. H.; Solomon, E. I. (unpublished work).
- (41) Gamelin, D. R.; Randall, D. W.; Hay, M. T.; Houser, R. P.; Mulder, T. C.; Canters, G. W.; de Vries, S.; Tolman, W. B.; Lu, Y.; Solomon, E. I. *Journal of the American Chemical Society* **1998**, *120*, 5246.
- (42) Bar-Nahum, I.; Gupta, A. K.; Huber, S. M.; Ertem, M. Z.; Cramer, C. J.; Tolman, W. B. *Journal of the American Chemical Society* **2009**, *131*, 2812.
- (43) Bhattacharyya, S.; Sarkar, A.; Dey, S. K.; Jose, G. P.; Mukherjee, A.; Sengupta, T. K. *Dalton Transactions* **2013**, *42*, 11709.